UNIVERSIDADE DE LISBOA

FACULDADE DE CIÊNCIAS

DEPARTAMENTO DE FÍSICA

Investigating the impact of beam and target parameters in particle imaging

Mariana Rodrigues Reis

Mestrado Integrado em Engenharia Biomédica e Biofísica

Perfil em Radiação em Diagnóstico e Terapia

Dissertação orientada por:

Prof. Dr. Nuno Matela

Prof. Dr. João Seco

2020

Resumo

Estima-se que o cancro é a segunda principal causa de morte a nível mundial sendo responsável por aproximadamente 9.6 milhões de mortes em 2018, globalmente correspondendo a 1 em cada 6 mortes[98].

Cirurgia, radioterapia e quimioterapia estão incluídas como alguns dos vários regimes de tratamento adequados dependendo do tipo de cancro, sendo, portanto, o seu correto diagnóstico um factor de elevada importância. Radioterapia externa é definida como o tratamento que consiste na administração de diferentes tipos de radiação ionizante como o raio-X, raios Gamma, protões ou partículas com carga, utilizados como fim a destruição das células tumorais. Este processo consiste no efeito direto provocado pela radiação na estrutura do DNA, mais especificamente na dupla hélice, provocando uma ativação de sensores de destruição no DNA de modo a causar necrose, apoptose ou produzir um efeito na mitose de forma a deformar as características normais do neoplasma[94]. Exisre também um efeito indireto de destruição através das espécies reativas de oxigénio produzidas pela radiólise de água. A radiação absorvida pelas células, medida em unidades Gray (Gy) é definida como a quantidade de energia depositada pela radiação ionizante numa massa de volume de tecido, sendo que o dano celular é tanto maior quanto maior for a radiação absorvida[85].

As partículas carregadas possuem distribuições de profundidade-dose diferentes quando comparadas com fotões. A grande maioria da sua energia é depositada nos milímetros finais da sua trajetória, quando a sua velocidade diminui, sendo este factor o que forma o pico de Bragg, definido como um pico de dose estreito e localizado. O alcance desta mesma partícula no material é observado na posição de paragem do pico de Bragg[91]. Procedendo ao ajustamento da energia das partículas carregadas é possível depositar com alta precisão as doses pré-prescritas no corpo do doente, levando a que haja um rácio alto de deposição de dose no volume alvo quando comparado com tecido saudável. A errada localização do pico de Bragg pode resultar tanto em overdose dos tecidos saudáveis como em subdosagem do alvo. Portanto, um desafio importante na radioterapia consiste em determinar a energia incidente necessária da partícula de modo a permitir uma alta ionização num lugar específico do corpo humano.

Em terapia externa de fotões e protões, anteriormente ao tratamento, uma tomografia computorizada de planeamento é adquirido, onde as estruturas são delineadas de modo a providenciar um mapa de densidade eletrónica que mais tarde é traduzida para valores de poder de paragem[71]. A prática clínica corrente consiste em adquirir os valores de poder de paragem no doente procedendo à conversão de unidades Hounsfield de uma tomografia computorizada de planeamento para poder de paragem relativo. O poder de paragem relativo é definido como o poder de paragem de um material comparado com o poder de paragem da água[43]. Esta conversão consiste na correspondência entre valores das unidades Hounsfield e poderes de paragem relativos a partir de uma curva de calibração[91]. Contudo, não existe uma relação física entre o coeficiente de atenuação mássica do fotão, medido pela tomografia computorizada de planeamento, e os valores de poder de paragem relativos o que leva a incertezas associadas a este método de conversão. Estas incertezas têm um grande impacto no alcance atingido pelas partículas calculado no scan de tomografia computorizada do doente e variam na ordem dos 3%. Portanto, margens de segurança são adicionadas à dose administrada ao doente que rodeia o volume alvo planeado de modo a assegurar um volume total clínico do alvo. Como esperado, devido a estas margens de segurança, um volume significativo de volume de tecido saudável irá também receber dose.

Radiografia e tomografia de partículas são ferramentas utilizadas para o planeamento de tratamento e verificação em terapia de partículas de maneira a permitir a visualização da parte do corpo que está a passar pelo scan. A maior vantagem associada à imagiologia de transmissão de partículas quando comparada com a estimação dos valores de poder de paragem relativos com raio-X, é a maior precisão desta estimação devido às medidas efetuadas à espessura equivalente de água percorrida pelos protões ou iões leves após percorrer o doente. Sendo que os valores de espessura equivalente da água estão relacionados com a valores integrados de poder de paragem relativos, os mesmos poderão ser obtidos, em três dimensões, através da reconstrução da tomografia computorizada das projeções medidas dos valores de espessura equivalentes de água[71]. Portanto, imagiologia de partículas permite a estimação direta de valores relativos de poder de paragem através de tomografia computorizada de partículas.

Não obstante, a dispersão múltipla de Coulomb, definido como processos de dispersão de Rutherford sofridos por uma partilha aquando da sua viagem na matéria, limita a qualidade de imagem devido à defleção angular e deslocamento lateral das partículas. Estas dispersões dificultam a predição da localização e ângulo da partícula a uma dada profundidade. De modo a melhorar a resolução espacial, é necessário identificar a posição e direção da partícula antes e depois do objeto assim como medir a sua energia residual individual recorrendo a sistemas de detetores. O detetor utilizado para esta investigação da tese está mais profundamente explicado na secção 4.2. Os algoritmos Most Likely Path (MLP) ("Trajeto mais provável") e Cubic Spline Path ("Trajetória de linha cúbica") foram propostos em imagiologia de partículas com objetivo de melhorar o problema associado à dispersão múltipla de Coulomb. Recorrendo aos algoritmos mencionados, o objetivo principal desta tese é, portanto, a investigação da qualidade de imagem de radiografia em função da energia inicial do feixe de partículas.

Uma vez que a dispersão múltipla de Coulomb afeta a precisão do algoritmo MLP afetando, portanto, a resolução espacial, tem sido proposto por vários estudos[21,32,42,69,88] o uso de iões de hélio como partículas geradoras de imagem devido ao reduzido efeito associado de múltipla dispersão de Coulomb. Além do mais, quando comparados com protões, os iões de hélio possuem menos dispersão de alcance o que significa que têm menos ruído associado à imagem com o mesmo número de partículas por pixel[32]. Juntando estas vantagens associadas e ainda mais o facto de que os iões de hélio sofrem menos fragmentação quando comparados com partículas pesadas, fez com que estas fossem as partículas escolhidas para imagiologia como estudo para esta tese.

O estudo de Amato et al. (2020)[5] demonstra que o uso de energias mais altas para o feixe de partículas provoca uma redução da dispersão múltipla de Coulomb levando a um aumento da resolução espacial. Contudo, um aumento de dispersão de alcance da partícula leva a que haja um maior nível de ruído na imagem. No mesmo estudo, apenas objetos homogéneos são estudados e no caso dos objetos heterogéneos a dispersão múltipla de Coulomb aumenta significativamente o ruído de imagem[25]. Consequentemente, sendo que ainda é desconhecido o comportamento da qualidade de imagem aquando do aumento da energia do feixe para casos reais de doentes, o objetivo principal desta tese é a investigação da qualidade de imagem de radiografia de iões de hélio em função da energia inicial do feixe de partículas, tanto para fantomas homogéneos como para heterogéneos. Um protótipo de detetor[68] foi utilizado para simular, com simulações Monte Carlo no software de simulações TOPAS, as radiografias de hélio e, seguindo o estudo de Amato et al. (2020)[5], um material degradador de energia (cobre) foi adicionado entre o dispositivo rastreador traseiro e o detetor de energia de modo a compensar os alcances mais elevados associados a maiores energias do feixe. Nesta tese, um fantoma homogéneo de água com três cubos de alumínio inseridos foi estudado assim como um fantoma de uma cabeça pediátrica[34] de modo a estudar casos mais realistas. As reconstruções de imagem foram realizadas recorrendo ao algoritmo desenvolvido por Collins-Fekete et al. (2016)[19] e a qualidade de imagem foi analisada para resolução espacial, rácio entre contraste e ruído e o ruído por pixel em relação à dose absorvida.

Os resultados desta investigação, com o intervalo de energias do feixe utilizado (200-325 MeV/u), envolveram uma melhoria total de 46% de resolução espacial com o aumento da energia do feixe de partículas, exceto para o caso de 325 MeV/u que não segue a tendência. Em relação ao rácio entre contraste e ruído, ocorreu uma diminuição de 42% à medida que a energia do feixe de partículas aumentava.

Concluindo, existe uma melhoria qualitativa e quantitativa em termos de resolução espacial nas radiografias de iões de hélio associada ao aumento das energias do feixe de partículas com a adição de um degradador de energia.

Palavras-Chave: Pico de Bragg, alcance, poder de paragem, dispersão múltipla de Coulomb, resolução espacial

Abstract

Cancer is known to kill an estimate of 9.6 million people in 2018[98]. Therefore, it is urgent to ameliorate the associated treatment, specifically radiotherapy. Particle therapy is a form of cancer radiotherapy exploiting the highly localized dose deposit of charged particles, the Bragg peak, for advanced sparing of healthy tissue. However, the highly conformal dose deposit also presents a great challenge as misplacement of the Bragg peak can result in severe overdosage of healthy tissue/underdosage of the target. Precise particle therapy hence requires advanced image guidance methods. This thesis focuses on particle imaging for image guidance in particle therapy.

A precise relative stopping power map of the patient constitutes a vital part for accurate particle therapy. Charged particle imaging can determine the stopping power both tomographically with particle computed tomography (pCT), or combining prior knowledge from particle radiography and X-ray CT. In terms of image quality improvement, image reconstruction becomes challenging for particle imaging owing to the existence of Multiple Coulomb Scattering (MCS) limiting image resolution (worse spatial resolution) and leading to increased image noise[20]. In order to improve the image quality, therefore, most likely path (MLP) reconstruction algorithms are performed, to ameliorate the problem of MCS. Tracking detectors of individual particles before and after the patient are required to use MLP algorithms. Moreover, an energy/range detector is also necessary to measure the particles' residual energy/range after the patient and to ensure RSP accuracy. Both heavier particles and higher beam energies reduce the effect of multiple Coulomb scattering, leading to a better path estimation. It is also noted, that for lighter ions, fixing the initial range maximizes the physical dose deposition to the patient while minimizing the image quality[91]. In this thesis, therefore the image quality of helium ion imaging with a recent prototype detector system is evaluated as function of the beam energy in detailed Monte Carlo simulations.

With this research project, factors, such as beam and target parameters, involved in increasing image quality were studied in particle imaging taking into account detector design. The idea was to investigate how to improve upon a state-of-the-art prototype scanner, allowing for higher beam energies. This will be accomplished by adding an adequate energy degrader to the detector, between the rear tracker and the energy/range detector. This degrader had its main aim to compensate for the longer range associated with more energetic ions. The main goal was to investigate the image quality as a function of initial energy behave, assuming a realistic detector model in the simulation. Helium ion beams at six different energy levels available at a clinical ion beam therapy facility (200 MeV/u to 325 MeV/u) were used to image two different phantoms: a water phantom with three aluminum cubes inside and an anthropomorphic pediatric head phantom. Monte Carlo simulations were performed using the TOPAS simulation toolkit. For path estimation, the Cubic Spline Path (CSP) was employed, which is a computationally efficient variate of the MLP. To reconstruct helium ion radiographic images the Maximum Likelihood Method used. This algorithm yields highly accurate radiographs without the need of prior knowledge. Further, the image quality was analyzed through the contrast-to-noise-ratio (CNR), per-pixel-noise and the Modulation Transfer Function (MTF), considering the absorbed dose.

The results of this investigation, considering the beam energy interval, involve a total spatial resolution improvement of 46% measured with increasing beam energy, except for the 325 MeV/u case which does not fit the trend. In relation to CNR analysis, a decrease of 42% was found as the beam energy increases.

In conclusion, there is a quantitatively and qualitatively improvement in terms of spatial resolution in helium-beam radiography with increasing beam energies with the addition of an energy degrader.

Key Words: Bragg peak, range, stopping power, Multiple Coulomb scattering, spatial resolution.

Contents

Acknowledgements

First of all, I would like to express my sincere gratitude to both my supervisors Prof. Dr. Nuno Matela and Prof. Dr. João Seco for all the support and availability throughout this year.

I would also like to share my appreciation for PhD student Lennart Volz, without whom I would not have been able to complete this research, and without whom I would not have made it through my master's thesis.

I wish to thank all the team members as well from the DKFZ that accompanied me during the internship and provided support and encouragement throughout my lovely stay in Heidelberg.

With many thanks to all the professors of Institute of Biophysics and Biomedical Engineering whose insight and knowledge into the subject matter provided me enough background knowledge through this major research opportunity.

Last but not the least, to my family and friends, I simply could not have this without your support. Vielen Dank!

List of Figures

List of Tables

List of Abbreviations

ADC: Analog-to-Digital Converter
AQUA: Advanced Quality Assurance project
CSDA: Continuous Slowing Down Approximation
CSP: Cubic Spline Path
CT: Computed Tomography
HU: Hounsfield Units
MCS: Multiple Coulomb Scattering
MLP: Most Likely Path
PMMA: Polymethyl Methacrylate
PMT: Photomultiplier Tubes
PSF: Point Spread Function
PSI: Paul Scherrer Institute
RERD: Residual Energy/Range Detector
RSP: Relative Stopping Power
SI: Internation System of Units
SRIM: Stopping and Range of Ions in Matter
SSD: Silicon Strip Detectors
TOF: Time-of-Flight
WEPL: Water Equivalent Path Lenght
WET: Water Equivalent Thickness

1. Introduction

1.1. Cancer and particle radiotherapy

Cancer is the second leading cause of death globally and is responsible for an estimated 9.6 million deaths in 2018. Globally, about 1 in 6 deaths is due to cancer[98].

A correct cancer diagnosis is essential for adequate and effective treatment since every cancer type requires a specific treatment regimen that encompasses one or more modalities such as surgery, radiotherapy, and chemotherapy. External radiotherapy is defined as a treatment where different types of beam ionizing radiation (X-Ray, gamma ray, protons or charged particles) are used to kill tumor cells. Radiation can directly affect the DNA structure of the double helix provoking the DNA activation of damage sensors in order to cause necrosis, apoptosis or to produce an effect on the normal mitosis process, rewiring neoplasm cells' biological characteristics[94]**.** There is also an indirect damage through reactive oxygen species produced by water radiolysis. Cellular damage increases with (absorbed) radiation dose (measured in Gray units, Gy) – the amount of energy that ionizing radiation deposits to a mass of tissue volume[85].

Charged particles have different depth-dose distributions compared to photons. They deposit most of their energy in the last final millimeters of their trajectory (when their speed slows). This results in a narrow and localized peak of dose, known as the Bragg peak, the 80% distal fall-off position of which defines the particle's range in matter[91] . By adjusting the energy of the charged particles one can deliver prespecified doses anywhere in the patient's body with high precision. This allows for a high ratio of dose deposition in the target volume compared to the healthy tissue. Therefore, a challenge usually consists in determining the necessary incident particle's energy to convey high ionization at a specific place in the human body.

1.2. Current clinical practice: X-ray imaging

In photon and proton external beam therapy, prior to treatment, a planning tomography scan is acquired and it is used to outline structures as well as a tool to provide a map of electron density translated afterwards to stopping power providing a source of error[71]. The current clinical practice consists on acquiring the stopping values within a patient performing a conversion from X-ray computed tomography (CT) Hounsfield Units (HUs) to Relative Stopping Power (RSP), defined as the stopping power of a material to the stopping power of water[43]. The conversion is carried out through a calibration curve which corresponds values of HU to values of RSP[91]. However, there is no physical relation between photon mass attenuation coefficient, measured by the X-ray CT, and RSP, leading to uncertainties associated to the mentioned conversion method. These uncertainties have a significant impact on the range that is calculated on the patient CT scan and they vary in the order of 3%. Safety margins are then added to the dose given to the patient, surrounding the planning target volume to ensure total clinical target volume. Usually these safety margins vary in the order of 2.5% to 3.5% of the particles' initial range with the addition of a constant margin value (1 to 3 mm)[62]. As can be expected, due to these safety margins addition, a significant volume of heathy tissue is receiving dose as well.

1.3. Potential Solution: Experimental modality of particle imaging

Particle radiography and tomography are promising tools for treatment planning and verification in particle therapy that enable visualization of the body part that is being scanned. By measuring the water equivalent thickness (WET) traversed by protons or light ions after traversing the patient, particle transmission imaging offers the potential for more accurate estimation of RSP inside a patient, which is the methods main advantage in comparison with x-ray based stopping power acquisition. The WET though the patient is related to the integrated RSPs. Hence, three-dimensional RSP values can be obtained through computed tomography reconstruction of the measured WET projections[71]. Therefore, particle imaging enables to estimate RSP directly in form of a particle computed tomography (pCT) or by combining a low number of projections with an x-ray CT. Note that for particle imaging much higher energies are required than used for tumor therapy. However, the RSP is nearly energy independent in the relevant energy range, such that the use of higher beam energies for particle imaging is not problematic[71].

On the other hand, MCS, that is the countless Rutherford scattering processes a particle undergoes while traveling through matter, provoking a lateral displacement and angular deflection of the particles, limits the achievable image quality. These interactions, the scatterings, complicate the location and angle prediction at a given depth of the particle. To improve the spatial resolution, in particle tracking imaging each particle position/direction before and after the object, as well as its residual energy, is measured individually. Various algorithms have been proposed in particle imaging, to ameliorate the problem of MCS, which estimate the particles' most likely trajectory through matter, for instance the Most Likely Path (MLP) algorithm and the Cubic Spline Path formalism better explained in section 3.1.2. of the state of the art. The path estimation accuracy depends on the precision associated to the particles' position and direction before and after the patient. Consequently, detector systems capable of tracking individual particles and obtaining their residual energy/range after the patient are mandatory. The detector setup is more profoundly explained in section 4.2. which was the detector setup we used for our actual simulation.

MCS affects the precision of the MPL as well, affecting the image spatial resolution. Therefore, various studies[21,32,42,69,88] have been proposing the usage of helium ions as image generating particles due to a lower MCS associated effect. In addition, when compared to protons, helium ions also have less range straggling (reduced by a factor of 2) which leads to a lower image noise at the same amount of particles used per pixel[32]. Furthermore, helium ions suffer from less fragmentation when compared to heavier ions, being ideal to be used as image generating particle species.

The study by Amato et al. (2020)[5] demonstrates that for higher beam energies a reduction of the MCS occurs leading to a spatial resolution increase. However, the increased range straggling comes with a higher noise level associated. In Amato et al. (2020)[5], however, only homogeneous objects are considered and in heterogeneous objects, MCS leads to a significant increase in image noise[25]. For this reason, it is still not evident how the image quality behaves with the increasing of beam energies for real patient cases. Consequently, the aim of this thesis was researching the image quality of helium ions' radiography as a function of initial beam energy both for homogeneous and heterogenous phantoms. A prototype particle CT detector system[68] developed for a maximum beam range of 260 mm, was used to simulate the helium radiographs. Further, following the work of Amato et al. (2020)[5], an energy degrader was added between the rear tracker and the energy detector to account for the longer ranges associated to higher beam energies. To corroborate the results from Amato et al. (2020)[5], a homogeneous test

phantom was also investigated. For more realistic cases in clinical terms, an anthropomorphic pediatric digital head phantom[34] was investigated. To perform the image reconstructions the radiography algorithm developed by Collins-Fekete et al. (2016)[19] was applied. Image quality was analyzed for spatial resolution, Contrast-to-Noise Ratio (CNR) and per-pixel noise versus absorbed dose.

2. Theorical Background

2.1. Interaction of particles with matter

2.1.1. Ionization

For charged particles at energies relevant for imaging radiotherapy, the main interaction process is ionization energy loss. This mechanism leads to ionization and atomic or collective excitation. Particle's range in matter can be determined by integrating over the particles' initial energy to zero (this represents the continuous slowing down approximation (CSDA)), calculated applying the Bethe stopping power equation (2. 1)[16]:

$$\langle -\frac{dE}{dx} \rangle = Kz^2 \frac{Z}{A} \frac{1}{\beta^2} \left[\frac{1}{2} ln \frac{2mec^2\beta^2\gamma^2 Wmax}{I^2} - \beta^2 - \frac{\delta(\beta\gamma)}{2} \right]$$

2. 1

where $K=4\pi N_A r^2_e m_e c^2$ and r_e corresponds to classical electron radius being equal to $e^2/4\pi\varepsilon_0 m_e c^2$. $\beta = v/c$ is the particles' velocity v and speed of light c ratio, ε_0 is the vacuum permittivity, the N_A corresponds to the Avogadro's constant, m_e the electron's mass and z corresponds to the charge of the incident particle. W_{max} corresponds to the maximum possible energy transfer to an electron in a single collision, A to atomic mass of the absorber and $\delta(\beta\gamma)$ to the density effect correction to ionization energy loss. As it is possible to observe looking into the equation, the stopping power depends on the incoming particle's kinetic energy, the mean excitation potential I, the atomic number of the absorber Z and the electron density ρ_e of the target. $\frac{dE}{dx}$ corresponds to the mean energy loss and is described by Bethe equation (2. 1) defined as Stopping Power S(x).

The particle's velocity decrease leads to an increase of the particle's mean energy loss which also corresponds to an increase of energy transfer at a deeper length in the target. Considering lower energies, in relation to the lower limit of Beth-Bloch's validity, the incoming particle's velocity is similar to the target atom's electron velocity, therefore, the particle can capture the electrons from the target changing Z to Z_{eff}[91] which is calculated from the empirical Barkas formula[6]:

$$z_{eff} = z.[1-\exp(-125\,\beta z^{-2/3})].$$

2. 2

The stopping region of the particles induces a narrow peak of the transferred energy, the Bragg-Peak, at the end of the particle's range in matter. This narrow peak allows an ideal dose delivery in ion therapy when compared to photon therapy, since it enables a localized dose deposition in the tumor area, largely avoiding excess dose to surrounding healthy tissue and organs at risk. The dose deposit is measured in gray (Gy) which is a derived unit of ionizing radiation dose in the International System of Units (SI). It is defined as the absorption of one joule of radiation energy per kilogram of matter[84].

When comparing a single particle with a beam of particles, the Bragg peak would be much sharper for a single particle than what can be experimentally measured for beam of particles. This is due to statistical variations in the energy loss of particles, also called as energy straggling, at a given depth. The energy straggling is originated by the stochastic nature of the energy transfer in a single interaction and, therefore, a different location to deposit the maximum dose. In order to cover a larger volume with a uniform dose, multiple Bragg peaks, i.e. multiple particle beams at different energies, are

superimposed, creating a so called Spread Out Bragg Peak (SOBP)[91]. This is represented in *Figure 2. 1*, as well as a comparison between dose curves for proton and photon treatments:

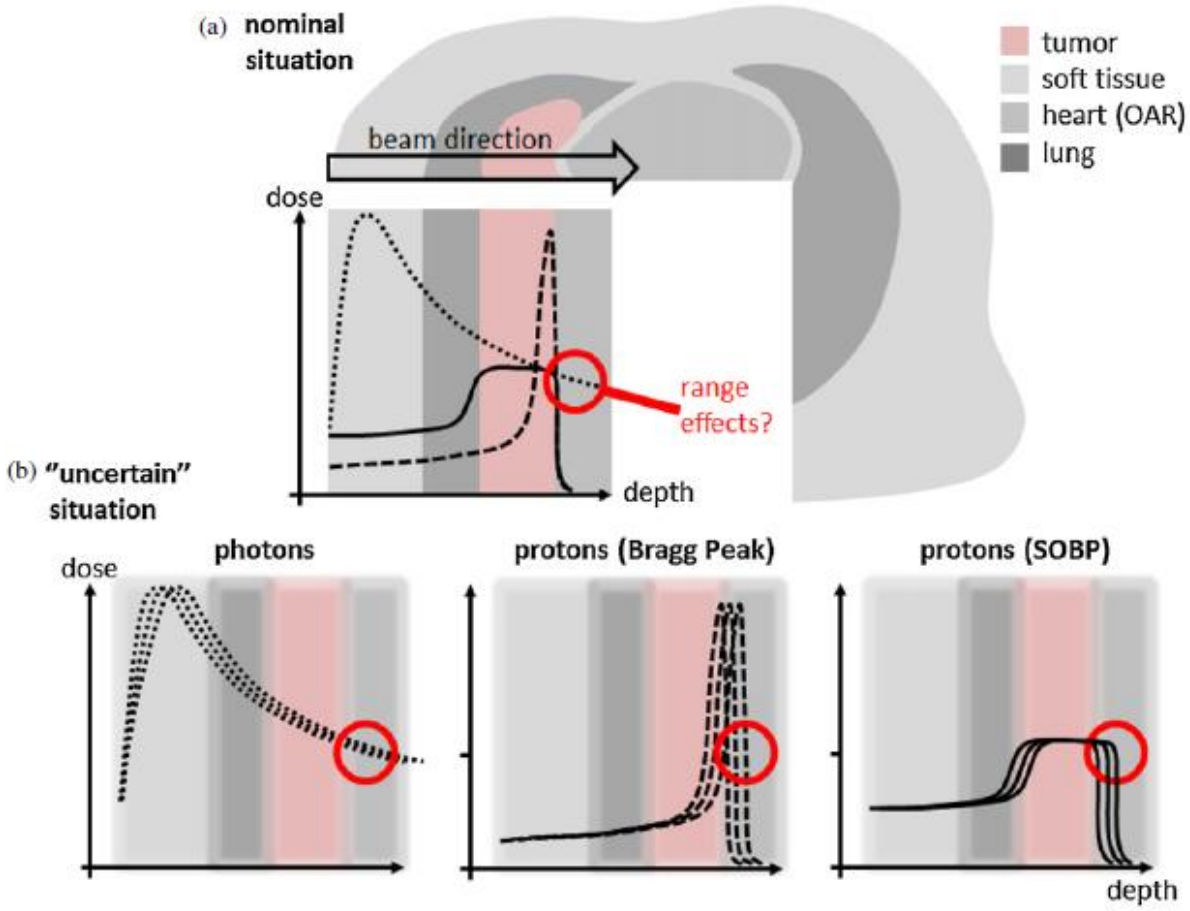

Figure 2. 1 (a) Proton treatment compared to photon treatment (the dotted line corresponds to the photon depth dose curve; the dashed line to the mono-energetic proton depth dose curve, the Bragg Peak; and the straight line to the SOBP to account for the totality of the tumor). (b) Uncertainties associated to the depth dose curves. Image taken from Knopf, A.-C. & Lomax, A (2013)'s work[52].

Furthermore, particle's interactions through matter lead to statistical variations in: lateral position at a given depth, called "scattering", particle direction at a given depth, called the "angular straggling", energy at a given depth, called the "energy straggling" and the stopping depth for a given initial energy, called the "range straggling"[71], as mentioned in the previous chapter. MCS predominantly causes the random deviations in particle direction leading to lateral deviations and these two types of straggling are correlated. This will be described in more detail in the following sections.

2.1.2. Range and thickness crossed

It is relevant to define important concepts related to interactions of charged particles with matter. Therefore, range can be defined as the depth in the target where the beam's mean kinetic energy corresponds to zero, where the Bragg-Peak is located. The particles' range depends on the initial energy, the particle type, the electron density, as well as the I value and the atomic charge and mass of the target

material [variables in equation (2. 1)]. The range of the incoming particles, R, can be calculated, using the Continuous Slowing Down Approximation (CSDA) as:

$$R= \int_{Ein}^{0} \frac{1}{-<\frac{dE}{dx}>} dE,$$

2. 3

where E_{in} and <dE/dx> corresponds to the initial energy and to the electronic energy loss as defined in equation (2. 1), respectively.

Relative Stopping Power (RSP) refers to the ratio of the stopping power of a material to that of water, being approximately constant in energy. It also simplifies the range to:

$$R_{mat}=R_{water}/RSP_{mat}$$

2. 4

where R_{mat} is the range in the material, the RSP_{mat} the RSP of the material and R_{water} the range in water which describes the incoming particles range in water[43].

The incoming particle's range can be converted to Range in Water (R_{Water}) as well as the target material thickness crossed which can be converted to Water Equivalent Thickness (WET) which permits an easier comparison between different setups in particle imaging. Therefore, the R_{Water} can be calculated as:

$$R_{Water}= \int_{Ein}^{0} \frac{1}{-<\frac{dE}{dz}>(Iwater,\beta)} dE$$

2. 5

and describes the particles' range in water where I_{water} is the mean excitation energy of water. The R_{Water} can be approximated by a conversion between range and energy as[11]:

$$R_{Water} \approx aE_{in}^{b}$$

2. 6

where a and b are constants with respect to protons in water with values of 0.00244 and 1.75, respectively.

Water Equivalent Thickness (WET) corresponds to the length a particle would have to travel to lose the same energy value but in water and it is calculated recurring to an integration of the stopping power of water over the particle energy loss[70,83]:

$$WET= \int_{Ein}^{Eout} \frac{1}{-<\frac{dE}{dz}>(Iwater,\beta)} dE.$$

2. 7

where E_{in} and E_{out} correspond to the particle's energy before and after travelling through the material, respectively. The I_{water} value was given in the ICRU Report 49[11].

2.1.3. Range Straggling

Statistical fluctuations in stopping depth for a specific initial energy, due to the statistical nature of a set of independent interactions, lead to a widening effect on the Bragg peak. This is referred as range straggling. Range straggling variance can be defined as[26]:

$$\sigma_R{}^2 = \int \left(\frac{dE}{dx}\right)^{-3} \frac{d\sigma}{dx} dE.$$

2. 8

The previous equation can be solved for the evolution of the range straggling variance as a function of the depth x in the material[63]:

$$\frac{d\sigma R}{dx} = 4\pi N e^4 \frac{z^{*2}(x)}{\frac{dE^2}{dx}(x)}$$

2. 9

where N corresponds to the target's electron density and z^* to the effective charge of the projectile.

In relation to the relative range straggling of a particle with energy E and mass M:

$$\frac{\sigma R}{R} = (M)^{-\frac{1}{2}} \Phi\left(\frac{E}{Mc^2}\right)$$

2. 10

where Φ is a slowly varying function, which has dependency on the target material. The previous equation allows for a useful scaling law to estimate the range straggling for particles with the same range:

$$\frac{\sigma R1}{\sigma R2} = \sqrt{\frac{M2}{M1}}$$

2. 11

Observing the above equation, it is possible to conclude that the relative straggling for C-ions is 3.5 times smaller than for protons. E.g. the straggling at 18 cm is closely 7 mm, which is too low to create a homogeneous target dose distribution in pencil beam scanning.

Range straggling is an important concept, because, with a longer range, associated to a higher beam initial energy, a higher range straggling is obtained leading to more noise in the image reconstructions.

Regarding image quality in particle radiography and tomography, straggling effects have an important influence on it. Every noise form is subject to the number of particles used for imaging (or the dose to the patient), therefore, a higher intrinsic variation of the WET information due to scattering and straggling, requires a dose to reach a certain noise level in the image. Moreover, energy loss straggling is caused by noise, energy detector resolution and MCS. In the scattering case, it influences and limits the spatial resolution and may result in image artefacts and noise. According to Amato, Martisikova and Gehrke, (2020)'s work[5], it is possible to decrease scattering effects by increasing the

initial particle energy. However, this increases the range straggling (since range straggling is proportional to the initial range of the particles), which increases the image noise[71].

2.1.4. Multiple Coulomb Scattering

For accurate image reconstruction in particle imaging, mitigating the particles' scattering is mandatory. Charged particles when traversing matter suffer a lateral spread of the initial beam, that is, a particle deflection in direction and angle, interacting with the target material through single Rutherford scatterings, the MCS[91] . Therefore, it becomes a challenge to precisely predict the location and angle at a given depth, for each particle.

In Moliere's theory case: the beam's lateral displacement and angular deflection follow a probability distribution which can be determined recurring to the Molière's theory. The theory describes the beam's phase space shape using a series of correction functions, and among those, the first and most important one, a Gaussian with width:

$$\theta = \frac{\chi c}{\sqrt{2}}\sqrt{B} \qquad 2.\ 12$$

B and χ_c are the angle per scattering and the mean scatterings number per particle, respectively, and both are calculated through the Molière's theory. For the small angle region cases, the distribution given by this theory behaves Gaussian, whereas for the larger angles case it follows $1/\theta^4$.

In Moliére, (1947)[57] and Moliére, (1948)[58] studies' it was possible to accurately predict the beam's lateral and angular spread in matter by solving the transport theory for a charged particle beam travelling a slab of an arbitrary material.

In Fermi-Eyges theory: primarily, Fermi presented the Gaussian approximation associated to MCS, which considered a connection probability of angle and position for a single incoming particle in a homogeneous material[74]. Following, in Eyges (1948)'s work[27], the energy loss of the particle was also included in relation to Fermi's theory. Consider a particle entering the patient as shown in *Figure 2. 2*. Since scattering in the two lateral directions can be considered independent statistical processes, the following is limited to a two-dimensional geometry. The other lateral direction can be described identically. The x-axis represents the beam direction, the lateral direction is denoted y. E_{in} is the initial kinetic energy of the particle, associated with a momentum p_{in} and velocity v_{in}. Fermi-Eyges theory uses a bi-variate (depending on both y and θ) Gaussian probability distribution, to describe the probability of finding the particle at depth x with a lateral displacement between y and y+dy and θ+dθ. This is given by Eyges, (1948)'s paper[27] as it follows.

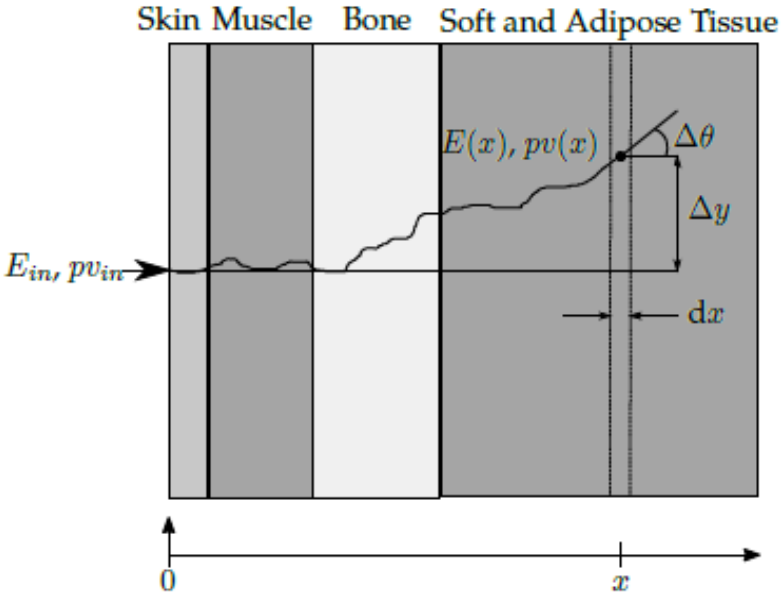

Figure 2. 2 Representation of skin, muscle, bone and soft tissue and adipose tissue addressing Fermin-Eyges theory. The x-axis represents the beam's direction. E_{in} is the initial energy of the incoming particle. Fermi-Eyges theory pretends to have a prediction regarding particle's lateral and angular displacement at a given depth x. Figure taken from Volz, (2017)[91].

$$P(y,\theta)\,dy\,d\theta = \frac{1}{\sqrt{2\pi B}}\exp\left(-\frac{1}{2}\frac{A0(x)y^2-2A1(x)y\theta+A2(x)\theta^2}{B}\right)dyd\theta \qquad 2.\ 13$$

where the A_n values ($n \in \{0,1,2\}$) are given as:

$$A_n(x)= \int_0^x (x-x')^n T(x')dx' \qquad 2.\ 14$$

and

$$B= A_0A_2-A_1^2. \qquad 2.\ 15$$

From Gottschalk (2012)'s work[37], A_n represent the variance in y, A_0, in θ, A_2, and A_1 is the co-variance of A_0 and A_2. Scattering power, represented by the variable T, is the change rate of the angular variance with the depth x and it is given by:

$$T(x)=\frac{d<\theta^2>}{dx} \qquad 2.\ 16$$

Scattering power not only depends on the target materials' local properties but also on the quantity of material the particles have crossed before reaching the depth x[37]. The gaussian approach is an approximation to MCS therefore, it is mandatory to define T in a way which best expresses Molière's theory.

One of the approaches available to the scattering power is the Highland T_H scattering power. With the aim of finding a better fit for the experimental data, Highland (1979) obtained:

$$T_H(x)=\frac{d<\theta^2 H>}{dx}=\frac{d}{dx}\left[\left(\frac{12.5MeV}{pv(x)}\right)^2\left[1+0.125\,log\left(\frac{x}{0.1X0(x)}\right)\right]^2\frac{x}{X0}\right].$$

2. 17

To account for the heterogeneous materials, Kanematsu, et al. (1998)[49] introduced an improved formula of the angular variance, based on equation (2. 17) as:

$$<\theta_{gH}^2>=[1+0.038\ln(\int_0^x\frac{dx\prime}{X0(x')})]^2\int_0^x\left(\frac{14.1MeVz}{pv(x')}\right)^2\frac{dx\prime}{X0(x')},$$

2. 18

where z accounts for the particles range, X_0 accounts for the material heterogeneity and $\int_0^x\frac{dx\prime}{X0(x')}$,the integral, and in general the logarithmic term account for the non-locality. Moreover, the $1/pv$ function accounts for the energy loss of the particles. For slower particles the MCS increases. Also, due to the proportionality of the $1/pv$ to mass, it can be seen from equation 2. 18, that the scattering variance scales with z^2/m^2 which means the standard deviation of the MCS is reduced by a factor 2 for helium ions when compared to protons. This is the main reason for using these ions for imaging.

MCS also results in image noise in heterogeneous objects, meaning it is not clear if increasing the beam energy will lead to an overall better image. The previous factor depends: from MCS viewpoint, higher beam energies will lead to better image quality, however, from the detector's viewpoint, higher beam energies are not favorable to the image quality. This is due to a higher range straggling and the need for a larger detector size. Basing on C. Amato (2020)'s[5] study, this project therefore will study the impact of increasing the initial beam energies and adding an energy degrader in the setup, on the image quality (being the images reconstructed using the Maximum Likelihood method described in the State of the Art section) and performing image analysis (Modulation Transfer Function (MTF), Contrast-to-Noise Ratio (CNR) , 2D noise maps and absorbed doses).

2.1.5. Helium Ions, nuclear interactions, and fragmentation

Nuclear interactions between particles and the target nuclei cause image noise in particle imaging[20,80] being necessary to be taken into account for a precise dose calculation in the treatment planning system[26]. Subdividing the nuclear interactions, they can be either coherent or incoherent where the first ones refer to interactions with the target core as a whole and the second ones refer to interactions with individual nuclei[38]. Coherent interactions can also be subdivided into elastic interactions and inelastic interactions, where the first ones consist of an approximately unvarying projectile's energy and a reduced quantity of retraction energy is delivered to the target, and the second ones where the excited nucleus, after collision, emits prompt γ, neutrons, protons, and alpha particles. The inelastic interactions add up to the image noise due to the projectile's scattering, therefore, filters are usually applied to reduce the particle angular displacement and to remove these interactions[81]. For the non-elastic interactions' case, the target and/ or primary particle usually suffer from fragmentation leading to the primary projectile's loss.

Primary ions, when travelling through matter, collide with other nuclei leading to nuclear disintegration. This process is denominated as nuclear fragmentation which produces secondary

particles (fragments) with a lower charge and energy when compared to the primary particles (e.g. protons and neutrons[91]). The secondary particles have a larger range in matter due to their smaller mass leading to a dose tail extension beyond the Bragg park, meaning, they overdose healthy tissues and produce image noise in particle imaging[91].

Moreover, as the depth of the object increases, the primary ions' loss (attenuation) increases as well as the amount of fragments produced. As the projectile charge increases, the total reaction cross section also increases for a given water thickness[78]. The cross section is defined as the probability to occur an inelastic reaction[24,53].

It has been proven that helium ions have a high associated spatial resolution and, due to the especially strong bond of the helium nucleus, are less likely to fragment compared to heavier ions[75,92] , having only six fragmentation channels. The expected fragment species for helium fragmentation are protons, deuterons, tritons and ^{3}He. This implies a less pronounced dose tail behind the Bragg Peak. Therefore, they are a good fit for particle imaging. However, it is still mandatory to identify and remove secondary particles to avoid problems related to image quality. In addition, according to Rovituso, et al. (2017)[75], at 8 cm of water depth, ^{4}He ions present a survive fraction 16% higher than ^{12}C ions[41], and at 20 cm of water depth, 65±5% of primary ^{4}He ions do not suffer fragmentation whereas only 38% of primary ^{12}C ions do not suffer fragmentation. This presents the clear advantage of helium ions for imaging. While carbon ions scatter less, the carbon ions increased fragmentation leads to an increased excess dose to the patient.

In terms of particle imaging, a mix between the primaries' energy loss and the lower energy deposit of fragments occurs due to the detection of the charged fragments in imaging systems with single-event registration[92], compromising the image quality. Therefore, filters are necessary to remove the fragment contamination before image reconstruction (e.g. Helium ions fragments, and the helium fragments (protons, neutrons, deuterons, tritium and ^{3}He)) to provide an increased image quality, for this reason, Volz et al. (2019)[93] have proposed a $\triangle$E-E filter for that task. In terms of treatment planning, the implementation of a lateral beam profile, which includes secondary particles in the treatment planning systems, is mandatory due to the high secondary fragments' angular distributions. These fragments transport dose away from the primary beam, either proximal to the tumor or lateral do the beam.

3. State of the art

Due to MCS, image reconstruction becomes challenging for particle imaging when compared to X-ray imaging. Therefore, acquiring the RSP map of the object also comes with limitations and, consequently, to retrieve the RSP accuracy of charged particle imaging, the image reconstruction is performed on a single-event basis processing each particle individually. Single-event reconstruction algorithms also perform a precise reconstruction of the particle's trajectory along the object. By improving path estimation algorithms, it is possible to acquire a better image reconstruction and to predict more accurately the RSP map.

Therefore, a literature review was made on the state of the art of the methods used to estimate the particle's path and image reconstruction in particle radiography as well contemporary instrumentation efforts for particle CT. Moreover, the state of the art also contemplates image quality analysis methods, the detector calibration procedure, techniques on improvement on spatial resolution and the △ E-E filter.

3.1.Path reconstruction algorithms

Different algorithms for accurate particle path estimation have been proposed in order to ameliorate the problem of MCS. The Most Likely Path (MLP) formalism and Cubic Spline Path (CSP) formalism will be presented.

3.1.1. The Most Likely Path (MLP) formalism

The first version of this algorithm, by Schneider and Pedroni (1994)[79] estimates the particles' most likely trajectory, including its standard deviation, in the matter, with the entrance and exit position of the incoming particle as known information. An improved version of the algorithm by Schulte, et al. (2008)[81] adopts the use of Bayesian statistics to estimate the maximum likelihood of the lateral displacement and the direction at a given depth within a homogeneous absorber.

In this improved version, the bi-variate Gaussian probability distribution given by Fermi Eyges-Theory (equation 2. 9) is evaluated in matrix form. For this, the particle lateral displacement y and angular displacement Θ are combined in a 2D parameter vector as:

$$Y = \begin{pmatrix} y \\ \Theta \end{pmatrix} \qquad 3.\ 1$$

y is the lateral displacement and θ is the direction at the point of interest while y_0 and θ_0 are initial entrance values. In this case, a parameter vector is defined as a collection of parameters forming a vector which represents coordinates (lateral displacement and direction at the point of interest) of a real space. The 2D vector measured at the entrance tracker at depth x_0 parameter vector is:

$$Y_0 = \begin{pmatrix} y0 \\ \Theta 0 \end{pmatrix}$$

3. 2

Similar, the parameter vector describing the exit measurement at depth x_2 is given as:

$$Y_2 = \begin{pmatrix} y2 \\ \Theta 2 \end{pmatrix}$$

3. 3

Where y_2 is the lateral position measured for the particle at the object exit, and Θ2 its angular displacement. Succeeding, the probability of finding a proton at Y given the entrance parameter vector is computed.

The likelihood function is calculated using the generalized Fermi-Eyges theory:

$$\mathscr{L}(Y|Y0) = \exp\left(-\frac{1}{2} Y'^{T} \Sigma_0^{-1} Y'\right)$$

3. 4

where Σ_0^{-1} is the inverse of the scattering matrix with the scattering moments A_n calculated using the following equation based on Fermi-Eyges theory already explained in section 2.1.4 above:

$$A_n = E_0^2\left(1+0.038 \ln \frac{(x-x0)}{X0}\right) \int_{x0}^{x} \frac{(x\prime-x0)^n}{p(x')^2 v(x')^2} \frac{dx\prime}{X0}$$

3. 5

where E_0 is an empirical constant equal to 13.6 MeV/c and A_n represents the scattering matrix elements as in:

$$\Sigma_0 = \begin{pmatrix} A2 & A1 \\ A1 & A0 \end{pmatrix}.$$

3. 6

Y' is the difference between the parameter vector Y and the entrance parameter vector propagated to depth x, i.e :

$$Y' = Y - R_0 Y_0$$

3. 7

and:

$$R_0 = \begin{pmatrix} 1 & x-x0 \\ 0 & 1 \end{pmatrix}$$

3. 8

Similar, the likelihood function of Y given the exit data parameter is obtained as:

$$\mathcal{L}(Y|Y2) = exp\left(--\frac{1}{2} Y''^{T} \Sigma_2^{-1} Y''\right)$$

3. 9

Where the parameter vector Y'' represents the difference between Y and the exit parameter vector propagated backwards to depth x as:

$$Y'' = Y - R_2 Y_2 \tag{3. 10}$$

but this time:

$$R_2 = \begin{pmatrix} 1 & x2 - x \\ 0 & 1 \end{pmatrix} \tag{3. 11}$$

Σ_2 is defined from the scattering moments A'_n describing the scattering from the exit position to the interest point. A'_n can be written as:

$$A_n' = E_0^2 \left(1 + 0.038 \ln \frac{(x2-x)}{X0}\right) \int_x^{x2} \frac{(x2-x')^n}{p(x')v(x')} \frac{dx'}{X0} \tag{3. 12}$$

This gives the scattering uncertainty matrix of the exit measurement Σ_2:

$$\Sigma_2 = \begin{pmatrix} A2' & A1' \\ A1' & A0' \end{pmatrix} \tag{3. 13}$$

Finally, the combined likelihood of finding a particle at depth x with a parameter vector Y, given both entrance and exit measurements is:

$$\mathcal{L}(Y|Y_0, Y_2) = \mathcal{L}(Y|Y_0)\, \mathcal{L}(Y|Y_2) \tag{3. 14}$$

The right-hand side of the equation (3. 14) then reads: the likelihood of the position/direction given the entrance measurement times the likelihood of the position/direction given our exit measurement. The most likely value for Y is found by maximizing the likelihood formalism (Maximum Likelihood Method):

$$Y_{MLP=} (\Sigma_1^{-1} + R_2^T \Sigma_2 R_2)^{-1} (\Sigma_0^{-1} R_0 Y_0 + R_2^T \Sigma_2^{-1} Y_2). \tag{3. 15}$$

3.1.2. Cubic Spline Path (CSP) formalism

Aside from the analytical formalism, which is demanding regarding the computation time, a phenomenological approach has been proposed by Collins-Fekete et al. (2015)[29]. This formalism based on cubic splines with optimized direction parameters greatly improved reconstruction speed. The CSP trajectory $\vec{S}$ can be calculated by:

$$S(K) = (2K^3 - 3K^2 + 1)\, \vec{X}_0 + (K^3 - 2K^2 + K)\, \vec{P}_0 + (-2K^3 + K^2)\, \vec{X}_2 + (K^3 - K^2)\, \vec{P}_2$$

3. 16

The vectors $\vec{X}_0$ and $\vec{X}_2$ are the entry and exit position, respectively, and $\vec{P}_0$ and $\vec{P}_2$ are the corresponding direction vectors[29]. K represents the depth within the object and belongs to an interval from 0 to 1, being 0 the entrance point and 1 the exit point of the target. K can be calculated at each depth x using the entrance point x_0 and exit point x_2 as:

$$K=\frac{x-x0}{x2-x0}.$$

3. 17

S(K) is a three dimensional vector which provides information regarding particles' position at a specific depth in the target.

The former formalism does not consider MCS, therefore, Hansen, et al. (2014)[42] introduced a new factor: $\overrightarrow{P'}_{0,2}=|x_2-x_0|.\ \hat{P}_{0,2}$, to scale the direction vectors by the thickness travelled by the particles. Collins-Fekete et al. (2015)[29] further extended this scaling, introducing phenomenological factors:

$$\Lambda_0^{opt}= 1.01+0.43(\frac{WET}{Rwater})^2$$

3. 18

$$\Lambda_2^{opt}= 0.99-0.46(\frac{WET}{Rwater})^2,$$

3. 19

since an increasing WET provokes an increase of the maximum position and angle deflections as well. Therefore, the normalized vectors were scaled as:

$$\overrightarrow{P'}_{0,2}^{opt}= \Lambda_{0.2}^{opt}\ |x_2-x_0|.\ \hat{P}_{0,2}$$

3. 20

and $\overrightarrow{P'}_{0,2}^{opt}$ are inserted in equation (3. 16) substituting vectors $\vec{P}_0$ and $\vec{P}_2$:

$$S(K)=(2K^3-3K^2+1)\ \vec{X}_0 + (K^3-2K^2+K)\ \overrightarrow{P'}_0^{opt} + (-2K^3+K^2)\ \vec{X}_2 + (K^3- K^2)\ \overrightarrow{P'}_2^{opt}.$$

3. 21

Figure 3. 1 below represents a comparison between the path reconstruction algorithms performed by Schulte, et al. 2008[81] and Collins-Fekete, et al. 2015[29]. In section 4.4 of the methodology section of this thesis is was also performed a comparison between the proton path through a homogeneous water phantom using the GEANT4 TOPAS simulation toolkit and the same particle path but reconstructed implementing the CSP, and this result is present in *Figure 5. 1* of the Results section.

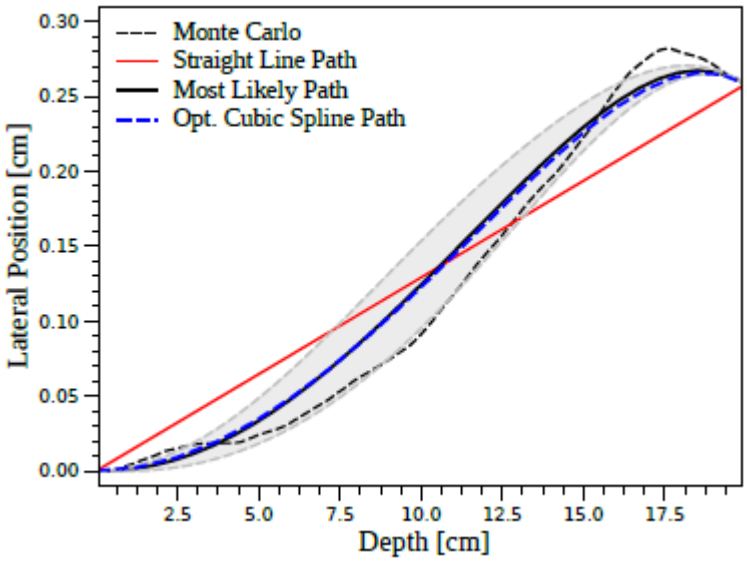

Figure 3. 1 Representation of the proton path (dashed-black) through a homogeneous water phantom employing the Geant4 simulation toolkit[1], as well as a path reconstruction of the latter using algorithms by Schulte, et al. 2008[81] (straight black) and by Collins-Fekete, et al. 2015[29] (dashed-blue). The grey area represents the standard deviation associated to the MLP algorithm. Figure taken from Volz (2017)[91].

3.2.Image reconstruction algorithms

In the literature, various reconstruction methods can be found for particle computed tomography and radiography. In this section, one approach is explained: The Maximum Likelihood formalism, which was mainly developed for radiographic imaging, ideally applicable for this thesis.

3.2.1. Radiography reconstruction: Maximum Likelihood reconstruction algorithm

The scattering suffered from the particles when crossing an object provokes a decrease in the spatial resolution (the further away the feature of interest is located from the tracker)[89]. Therefore, to improve the spatial resolution, MLP based algorithms have been proposed in the literature. The chosen algorithm for this thesis was the maximum-likelihood reconstruction method by Collins-Fekete et al. (2017)[21], being described in more depth below in this section. Another algorithm using the MLP is the plane-of-interest binning which consists of using the particle's MLP at the depth of the feature of interest to bin the particle into a 2D image plane[32,73]. As the feature's depth is required to be known for the latter algorithm, the preference for this thesis lied on the algorithm proposed by Collins-Fekete et al. (2017)[21].

In Collins-Fekete, Brousmiche, Portillo, Beaulieu, & Seco, (2016) 's project[19], a maximum likelihood least radiography's square estimator, that improves proton spatial resolution, was applied to the reconstructed images of different phantoms. Firstly, this method discretizes the object into channels corresponding to the image pixels (see *Figure 3. 2*). The WET of a particle is distributed into a pixel channel, if at least part of its estimated path lies within the channel boundaries. The WET of each channel is then calculated using a maximum likelihood estimator over all protons binned to the channel as explained in the following.

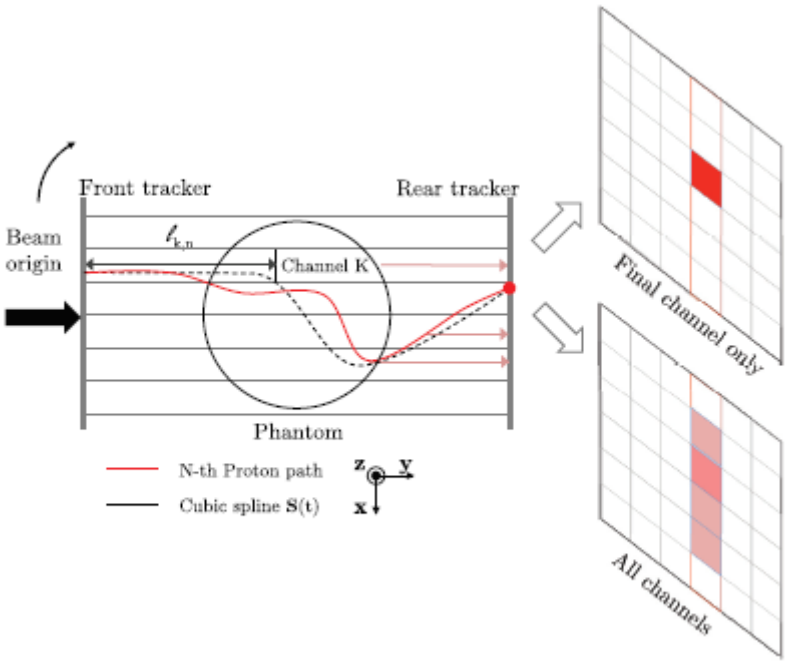

Figure 3. 2 Schematic view of the scanned phantom. The red line corresponds to the proton path and the dotted-line corresponds to cubic spline path estimate. The right side of the image represents the output from this technique. Figure taken from Collins-Fekete, Brousmiche, Portillo, Beaulieu, & Seco, (2016)[19].

To facilitate the understanding involved on this method, a few concepts are listed here: $l_{k,n}$ is the length crossed in channel k by the proton with index n. L_n is the total length which corresponds to the sum of $l_{k,n}$ over all channels crossed. Finally, the total WET of a proton is WET_n. Equation (3. 22) relates WET_n measured by the n^{th} proton to the WET of the k^{th} channel, the WET_k, through an error variable $v_{k,n}$.

$$v_{k,n} = WET_n - WET_k$$

3. 22

Equation (3. 22) has the main aim to estimate the WET_k which maximizes the likelihood of the proton's energy. $v_{k,n}$'s standard deviation is inversely proportional to the length travelled in k channel. The previous equation, subsequently, is multiplied by $l_{k,n}$ to retrieve homoscedasticity (defined as an identical errors' standard deviation over all possible value of $l_{k,n}$):

$$\epsilon_{k,n} = \frac{lk,n}{Ln}(WETn - WETk).$$

3. 23

Considering the likelihood estimator, the total likelihood of ϵ_k (ϵ_k is the error distribution particular to the k^{th} channel, while $\epsilon_{k,n}$ corresponds to a single realization of this error distribution for the n^{th} particle) and σ^2_k, given an N sized sample, can be represented in equation (3. 24):

$$\mathscr{L} = \prod_n^N N(\epsilon_k; 0; \sigma^2_k)$$

3. 24

The maximum likelihood estimator can be obtained taking the first derivate of log($\mathscr{L}$) with respect to WET_k. The final equation to obtain WET_k (equation (3. 25)) is acquired setting the log likelihood to zero[19]:

$$WET_k = \frac{\sum_n^N \frac{l^2 k,n}{Ln^2} WEPLn \frac{1}{\sigma^2 k}}{\sum_n^N \frac{l^2 k,n}{Ln^2} \frac{1}{\sigma^2 k}} = \frac{\sum_n^N \frac{l^2 k,n}{Ln^2} WEPLn}{\sum_n^N \frac{l^2 k,n}{Ln^2}}.$$

3. 25

In other words, the optimized WET of channel k is obtained as the weighted mean over the WET information of all particles crossing into the channel, where the weights correspond to the fraction of the particles path length spent in the channel. The result is an optimized WET radiograph, which yields an improved spatial resolution over the naive approaches (front tracker binning and rear tracker binning), but does not require prior knowledge on the object to be imaged.

The maximum likelihood estimator was applied in Collins-Fekete, Brousmiche, Portillo, Beaulieu, & Seco, (2016) 's study[19] to the reconstructed images of different phantoms: a slanted cube in a water tank to measure 2D spatial resolution, a voxelized head phantom (for clinical performance evaluation) and a Catphan phantom (CTP528) for 3D spatial resolution. The proton radiographies of each phantom were obtained recurring to GEANT4 Monte Carlo simulations[1] and the optimized proton radiography values represent the WET projection through a channel (a voxel projection). In conclusion, the maximum likelihood method applied improved significantly the spatial resolution from 3.49 lp cm^{-1} to 5.76 lp cm^{-1} representing a gain of 65%. The principal advantage associated to this technique, when compared to several reconstruction techniques, is that creates an improved proton radiography independent of the pCT reconstruction.

3.3.Instrumentation for proton radiography and tomography

In general, particle computed tomography systems consist of a combination of tracking detectors placed before and after the patient to acquire the particle path information and an energy detector that measures each particle's residual energy/range to infer the WET it crossed through the object. Different detector technologies have been proposed in the literature, where key focus lies on increasing the data acquisition rate the system can handle and the optimizing the accuracy and precision of the energy/range measurement. With contemporary prototype technology, a proton radiography can be acquired in seconds contrary to proton tomography which is acquired in minutes.

There are two important general requirements regarding pCT performance for the detectors: they should be able to handle at least 1×10^6 protons/s and should be about 30 cm in the longitudinal dimension for a head scanner, however, larger dimensions are mandatory for body scans[8]. Plastic scintillation detectors are the optimal choice due to their low-priced value and its fast intrinsic signal decay time ($\simeq$ 10 ns). Moreover, they are quite fast with suitable readout (usually photo-multiplier tubes) and its near water equivalent thickness makes them ideally suited for dosimetry[9].

A phase II prototype pCT system was developed in the United States by the US pCT collaboration with Loma Linda University, University of California Santa Cruz and California State University San Bernardino collaboration as well. High quality helium ion imaging with this protype has been demonstrated in Volz (2017)'s study[91]. The prototype consists of two Silicon Strip Detectors (SSD), being the tracking detectors, located before (front tracker) and after (rear tracker) the object that

is imaged, a five-stage energy/range detector hybrid with fast plastic scintillators, a platform that rotates giving full CT scans, and a high-speed data acquisition module with 14 Field-Programmable Gate arrays. The SSDs allow a high efficiency for charged particle detection and high spatial resolution (228 μm strip pitch). The tracking planes each contains two boards with four single sided SSD sensors, therefore, 8 SSDs boards in total. A 2D position measurement is possible due to two adjacent SSD with strip direction running in orthogonal direction. In relation to the energy/range detector, it measures the energy loss employing a combination of a range telescope and an energy calorimeter. The five-stage design allows a lower requirement of the energy resolution for each single stage, allowing the use of fast plastic scintillators, while retaining a WET resolution close to the particles range straggling. Each of the five stages is 5.1 cm thick and consists of UPS-923A polystyrene based scintillator stages read out by R3318 Hamamatsu photomultiplier tubes. Therefore, if a particle completely crosses a stage, the WET of the mentioned stage will contribute to the particles' residual range measurement, and only in the stage where the particle stops its energy needs to be measured relaxing the precision requirement. The energy deposit in the final stage reached by the particle is converted to the WET the particle has crossed in traveling through the object by means of an energy to WET calibration[91]. Below, there is a visual representation, in *Figure 3. 3*, of the phase II prototype in the HIT used in Volz (2017)'s[91] experiments. *Figure 3. 3* has the principal prototype's elements identified (front and rear tracker, rotating platform, and the energy detector).

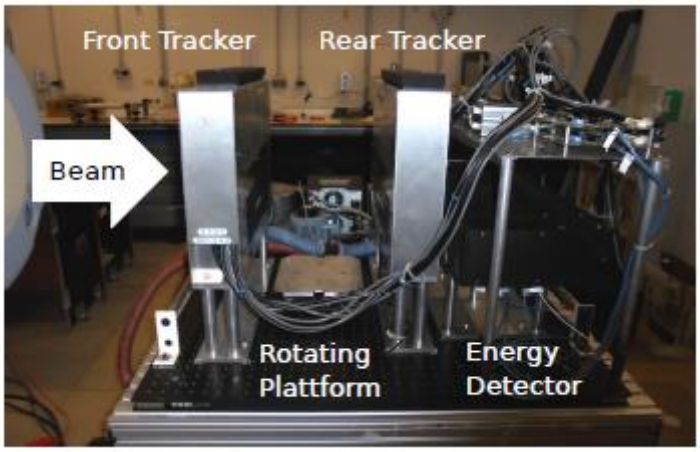

Figure 3. 3 Phase II prototype in the HIT facility. The front and rear tracker are aluminium boxes and the energy detector is a black box after the rear tracker. There is also a rotating platform in between the trackers. Image taken from Volz, (2017)[91].

A radiography instrument developed in Paul Scherrer Institute (PSI)[64] in the late 1990s is still used as a prototype to make tomography scans detecting protons one by one. A scintillating fiber hodoscope with two overlapping layers of 2 mm square fibers is used for the tracking layers of the instrument. Therefore, the tracking detector pixel pitch is 1 mm. The fibers are read out by a 16-channel Photomultiplier Tube (PMT). The PMT consist of a 4 x 4 array of independent photocathode and dynode chains. The combination of signals from the two overlapping layers identifies the coordinates of y or z. This configuration manner provides the advantage of a higher speed readout since it reduces the number of readout channels and data volume. The range telescope of this instruments is a stack of 64 three-millimeter plastic scintillator tiles read out by wavelength fibers connected to PMTs and the proton range is acquired according to the last pair of tiles which produced the signal. The main limitations associated to this instrument are that each tracker is composed by only a single detector layer in each

view and therefore, it just provides a point instead of a vector limiting the definition of the MLP of a proton[19,47].

More recently, the same authors of the PSI instrument mentioned above, developed a system for beam monitoring and particle radiography called "QBeRT" with similar technology as the PSI instrument, but instead read out by Multi-Pixel Photon Counters. It also includes a two-layer tracker and a range detector with scintillating fibers[31,72]. Moreover, it handles a fluence of 10^9 particles per second in verification mode and 10^6 particles per second in radiography imaging mode. Tests have shown good results[47].

Advanced Quality Assurance project (AQUA) is another proton radiography instrument, developed at the TERA foundation[4,14], with a tracking based on 30 cm x 30 cm GEM detectors[77]. It is a pixelated detector operating with gain from electron multiplication by a gas located in front of the range detector. The range detector is a 48 three-mm stack of scintillator planes each coupled by a wave-shifting fiber to an SiPM and 12-bit pipelined ADCs digitalize the signals individually allowing a throughput of a million events per second. There are still no published results regarding this system[47].

3.4.Calibration

Accurate WET reconstruction requires to calibrate the detector system prior to the imaging runs. In Piersimoni et al. (2017)'s paper[68] a Monte Carlo study was performed investigating the accuracy achievable with different calibration schemes for the pCT collaboration phase II prototype. The pCT scanner was simulated in three different configurations: an ideal totally absorbing, ideal detector, a single stage, and a multi-stage detector. The calibration of the pCT scanner had to be performed to convert the response of the residual energy/range detector directly to WET. The residual energy/range detector is used to measure the exiting energy to obtain the WET for each path.

In Piersimoni et al. (2017)'s paper [68] the pCT energy detector was simulated with three configurations, like mentioned above: configuration A consisted of no energy detector present in the simulation and each proton's energy loss was calculated as the difference between the front and rear trackers. Configuration B consisted of a single stage plastic energy detector and, finally, in configuration C it was used a five-stage scintillator which reproduces the multi-stage scintillator (MSS) of the pCT phase II scanner.

In relation to the WET calibration procedure in Piersimoni, et al. (2017)'s paper[68], a simulation of a polystyerene step phantom was performed to obtain calibration curves for configurations A and B. The step phantom consists of three pyramids along the x-axis direction and provides polystyerene thickness variation from 0 to 50.8 mm in the beam direction. Due to the range of WET that can be imaged with 200 MeV protons, four 50.8 mm removable polystyerene bricks were successively joined to the phantom's variable part throughout the calibration procedure. The WET of the bricks was obtained by range pull-back of a 200 MeV proton beam measured in a water column (PTW peakfinder, Freiburg, Germany).

For configuration A and B, the calibration simulation was carried out in five separate runs. The first run was dedicated to compile data for the stairs parts of the step phantom. In the remaining four runs the four bricks were added successively. Subsequently, 41 known WET step-lengths were accounted for. Each WET value was considered as being the air and polystyerene path lengths sum multiplied by their corresponding relative stopping powers. These last values were binned in 41

calibration points, each corresponding to the energy distribution mean value, associated to a specific WET value.

For the C configuration, two methods were used to execute the WET calibration: the first one used the same step phantom used for A and B configurations and for each calibration point an evaluation was made on the average energy deposit in the stage where the proton stopped relating it to the calculated WET. The second method used two polystyerene wedges instead of the step phantom stairs. Contrary to before, this method provided continuous WET distributions for each detector stage where the proton stopped. In the calibration processing, firstly the stage where the particle stopped (stopping stage) is identified. The stopping stage is the last stage in beam direction where an energy deposit higher than the noise threshold applied to the stage (1 MeV) is measured. Thereafter, the energy deposit in the stopping stage, and the known WET the particle crossed through the calibration phantom (known from the tracker measurements and the known geometry and RSP of the phantom) are binned into a 2D histogram corresponding to the stopping stage. After this has been performed for all particles contained in the calibration run projections, for each specific energy deposit in the stopping stage (in steps of 1 MeV for helium ions and 0.25 MeV for protons), the related most likely WET crossed by the particle is computed. The most likely WET corresponds to the peak WET in the histogram for the given energy step, i.e. the WET that most particles with this specific energy deposit in the stopping stage crossed.

In conclusion, in Piersimoni, et al. (2017)'s paper[68], the average WET error obtained from the WET calibration curve for configuration A was 2.08 mm and for configuration B was 2.21 mm. Moreover, by using the WET calibration procedure with the step phantom there were circular artifacts in the reconstructed image. The usage of the wedge calibration lead to a decrease of the artifacts of 0.4 %. This calibration procedure was therefore chosen also for this thesis.

3.5. △E-E filtering

In Volz, et al. (2018)'s study[92], the potential of using the △E-E filter with the aim of removing nuclear interactions in helium ion CT was analyzed. Nuclear interactions can provoke an unusual energy loss as well as secondary particles production which subsequently will add to the image noise and inaccuracy of RSP[80]. Therefore, data filters are necessary to identify and remove these specific events, i.e. fragments both arriving from the object and generated within the detector, from the particle histories. In most contemporary investigations, this is based on 3σ filters acting on the angular and WET distribution of the particles. The 3σ WET filter performance was firstly analyzed in order to investigate the △E-E filtering technique.

The main aim of Volz, et al. (2018)'s study[92] was investigating the accuracy associated to data filters in removing events where nuclear interaction occurs. Therefore, a comparison was made of image accuracy in between simulations with only electromagnetic interactions involved. Events which underwent an inelastic nuclear interaction were also counted before and after the filtering.

Filters involved in the data processing of Volz, et al. (2018)'s work[92] can be divided into two different types: the pre-calibration and the post-calibration filters. The first ones act on the energy loss measurement in the multistage detector right before energy loss conversion to WET, the latter conducted through the WET calibration procedure from configuration C in Piersimoni, et al. (2017)[68]. The second ones refer to the data filtering after the calibration procedure of the detector.

In relation to current pre-calibration filters, the first stage where the particle stopped was called the Bragg-peak stage with energy E. Events which had a higher energy deposit than predicted by a single proton in the Bragg-peak stage were eliminated in the pre-processing procedure. Stage thresholds were defined and all events for that the energy deposit in any stage leading to the Bragg-peak stage was lower than the stage threshold, were discarded. The energy loss of a particle in a △E stage and the particles' residual energy measured in another stage immediately after is unique to each particle species. This is due to the dependence of the stopping power on the mass and charge of the projectile. Consequently, △E-E telescopes are often used for particle identification of the spectral lines for each particle specie. The △E-E filter exploits this relationship by parameterizing the expected △E-E response for a primary particle. Any event for that the △E-E response does not agree with that of the primary within certain (user defined) margins is removed before image reconstruction. Moreover, the primary helium curve was parametrized with a second order polynomial function, making it possible to use the latter as a filter for secondary fragments in the image data pre-processing[92].

In relation to post-calibration filters, the events that were not removed by the filters mentioned above, were converted to WET values. The 3σ WET filter was then applied within the image reconstructions.

Considering the results obtained by Volz, et al. (2018)[92] the △E-E filter combined with the current pre-calibration filters, reduced the WET distribution tail, allowing a closer resemblance to the distribution where nuclear interactions were discarded and providing a more effective filtering by removing the secondary fragments, i.e. the ^{3}He fragments. This resulted in an improved RSP accuracy towards the reference value. In addition, it was also concluded that both △E-E and 3σ filter should be combined for the filtering procedure.

In *Figure 3. 4* it is possible to observe the △E-E spectrum where the △E-E filter was added to the current pre-calibration filters. In *Figure 5. 6* of the Results, it is also possible to observe the △E-E spectrum used for this thesis' simulations which was acquired following Volz, et al. (2018)'s study[92].

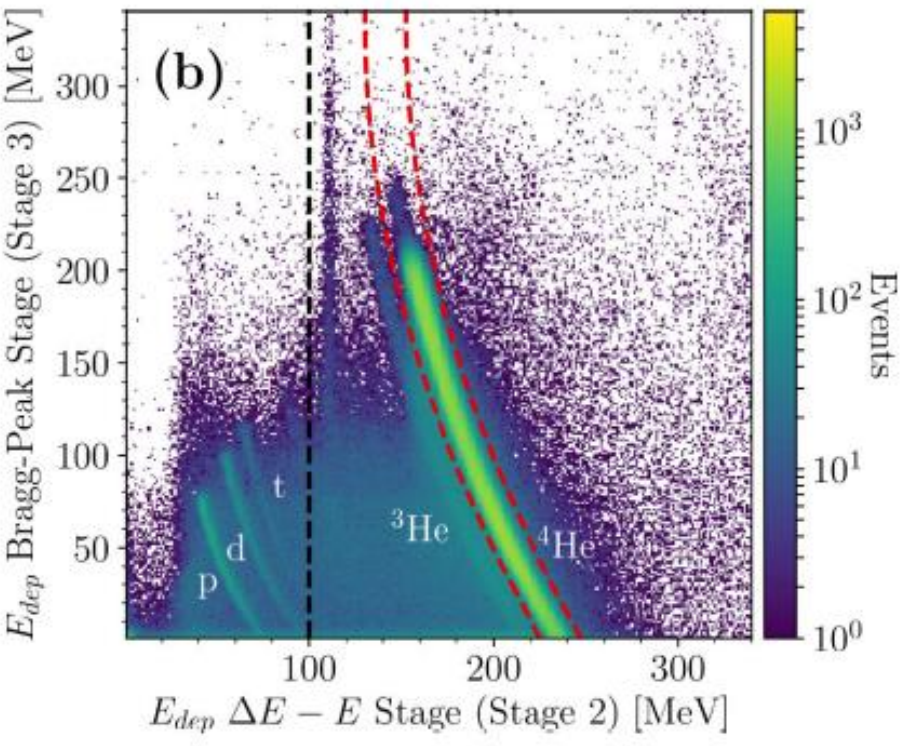

Figure 3. 4 △E-E spectrum: △E-E filter added to the current pre-calibration filter. Image taken from Volz, et al. (2018)[92].

3.6. Spatial resolution improvement in helium-beam radiography

In Amato, Martisikova and Gehrke, (2020)'s work[5], a technique is developed to improve the spatial resolution in helium-beam radiography that ebales the use of higher helium-beam energies to utilize the associated decrease of the MCS[47].

The research of Amato, Martisikova and Gehrke, (2020)[5] was executed with a single-ion tracking imaging system in an ion radiography system composed of pixelated silicon detectors. The energy deposition in an additional thin detector is measured and the various WET values associated to the imaged object are measured as different energy depositions. The irradiation was performed with increasing energies (168.8 MeV/u – 220.5 MeV/u) to image a Polymethyl Methacrylate (PMMA) phantom.

Moreover, in between the rear tracker and the energy detector an energy degrader was positioned, to compensate the larger range of the particles at higher energies, and to track ions at a high velocity when exiting the phantom before being slowed down by the energy degrader. The energy degrader thickness increases with the increasing of beam energy to keep the rising part of the Bragg peak at the energy-deposition detector to optimize the sensitivity to small WET value changes. Additionally, the energy degrader thickness optimization was performed, for each beam energy, recurring to Monte Carlo Simulations to satisfy the operating principle of the system. In relation to the energy degrader ideal properties, it needs to have a high RSP in order to maintain a low thickness of the system and it is also important to consider that MCS also accurs in the energy degrader. Therefore, the chosen material in this study was copper since it fitted in the requirements.

The Monte Carlo simulations were performed to optimize the energy degrader's thickness and beam energy. For around 170 MeV/u beam energies, no energy degrader was added and the position between the Bragg peak and the detector which measures the energy deposition was adjusted by only changing the beam energy. In this case the beam energy was varied in seven steps between 167.1MeV/u - 170.6MeV/u. For higher beam energies the energy degrader is required and the position between the Bragg peak and the detector which measures the energy deposition was adjusted by changing the degrader thickness at a fixed beam energy. For the three used energies (185, 202.4 and 220.5 MeV/u), with the SRIM software[101], an initial guess on the degrader's thickness was performed and subsequently varied in 8 mm steps. For each tracked ion, the path inside the phantom was reconstructed using the optimized Cubic Spline path[21].

To assess the effectiveness of the technique, for each investigated beam energy the contrast-to-noise ratio (CNR), the Water Equivalent Thickness (WET) precision and the dose absorbed by the phantom were investigated as a function of the energy of the initial beam. The spatial resolution was investigared for the the different beam energies, by using a tilted edge (with respect to the pixels)[30] to obtain the edge profile. Subsequently, the edge profile was fitted with an error function, and the Fourier transform of that error functionyielded the MTF as in Gehrke, et al. (2018)[32].

In conclusion, the spatial resolution indeed was demonstrated to increase with incrising energy for the beam energy range in Amato, Martisikova and Gehrke (2020)'s study[5]. They report a spatial resolution increase a 29% for the highest compared to the lowest beam energy in the investigated interval whereas in simulations, the spatial resolution was expected to increase by 34%. In general, experimentally, using higher helium-beam energies and an energy degrader it is observed an increase of spatial resolution with an acceptable CNR decrease of 22% in 1 mm pixel size radiographs. The method used in this study is not restricted to the same setups being also applicable to other single-ion tracking

systems, such as the one used in this work (described in the following section), being Amato, Martisikova and Gehrke, (2020)'s method[5] its main investigation point.

4. Methodology and materials

4.1. TOPAS Simulation Toolkit

TOPAS release 2.0[67] is a Monte Carlo simulation tool based on Geant4 version 9.6, which provides a better understanding regarding radiotherapy and imaging. Geant4 is a toolkit for Monte Carlo simulation of detectors in high energy physics[1,2,3]. TOPAS allows for simulations of ionizing radiation though multiple targets and patients, as well as detector system geometry simulation. It can also record dose and other quantities allowing an accuracy increase while reducing side effects in terms of radiation therapy treatments. The tool has as main target medical physics, radiobiologists, and clinicians[28,66].

4.2. pCT Scanner simulation on TOPAS simulation toolkit

The pCT scanner used for the simulations performed in this thesis was based on the pCT phase II scanner from Bashkirov, et al. (2016)[8] and the TOPAS implementation was created by Piersimoni, et al. (2017) [68]. The pCT scanner consisted of four position-sensitive detector modules (tracker system) to infer particle's path and a Residual Energy/Range Detector (RERD) consisting on a multi-stage scintillator (MSS) with a stack of five fast plastic scintillators read out by five (each for each stage) photomultiplier tubes. Each of the five stages was a 5.08 cm thickness polystyerene block. Each tracker (front and rear) included two tracker planes each with transversal and vertical coordinates.

The 5-multistage energy detector was defined, and each stage of polystyerene was set as an energy deposit scorer to obtain information regarding particle's energy loss measuring the exiting energy to determine WET for each track. The four position-sensitive detector modules (the silicon boards) were set as phase space scorers to provide the direction and coordinates for the detected particles. The TOPAS simulation of the pCT scanner is represented in *Figure 4. 1* below, where the white contoured parallelepipeds with the white and green planes inside represent the tracker system with the tracker planes inside and the yellow parallelepiped represents the MSS read out by the five blue photomultiplier tubes.

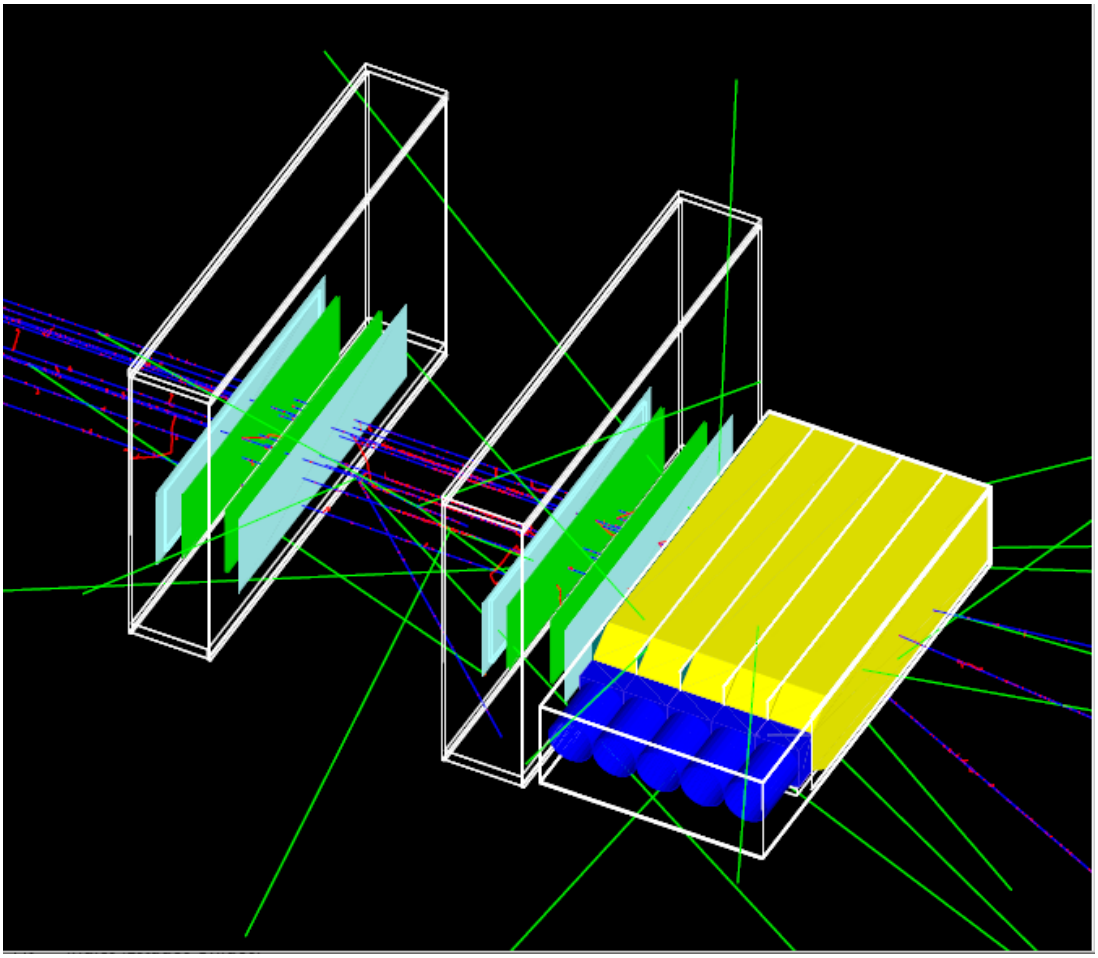

Figure 4. 1 TOPAS simulation of the pCT scanner used with the front and rear tracker (white contoured parallelepipeds) followed by the MSS (yellow parallelepiped). Image taken from Volz, L. (2020)[90].

As beam particles, helium ions (alpha particles) were used. The beam was delivered as a rectangular, ideal field (homogeneous fluence distribution, parallel particle directions). The beam kinetic energy was set to 200 MeV/u, 225 MeV/u, 250 MeV/u, 275 MeV/u, 300 MeV/u and 325 MeV/u energies. The scanner prototype was originally developed for the use with a 200 MeV particle beam (a range of 26cm).

The positions where the particle hit in the tracker as well as the energy deposit in the detector stages were stored as n-tuples. The analysis software runs under the *ROOT* data analysis framework[13] and includes scripts that use the TOPAS simulated data according to detector parameters already predefined. The *ROOT* data analysis framework allowed for the data unfolding (the radiograph image reconstruction) as well as the data writing into a txt file possible to reconstruct as an image from the radiograph.

The simulated phantoms in this work included a test phantom which consisted of a 15 cm thickness and 8 cm lateral width water cube with three 10 mm width aluminum cubes located in the center of the phantom and equally distanced between each other (as represented in *Figure 4. 2*), and a digital female anthropomorphic pediatric head phantom, showing the inferior part of the head, developed in Giacometti et al. (2017)[34]. A phantom was also created with the same dimensions as the head phantom in order to obtain its dose deposit.

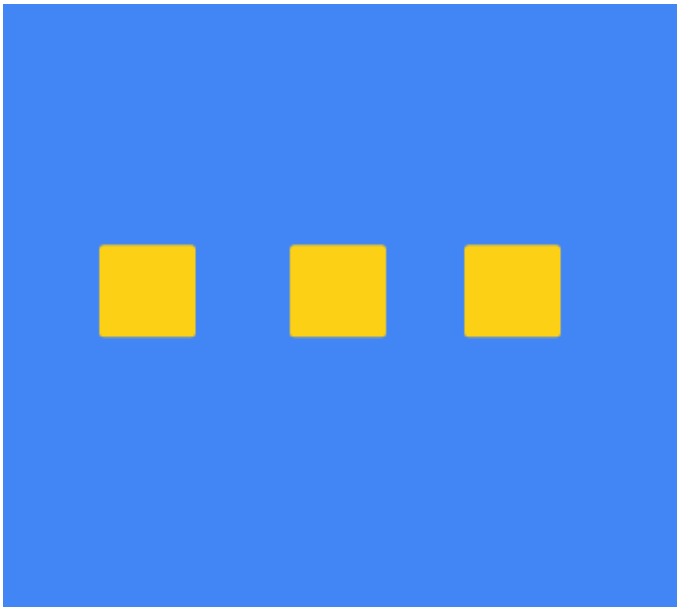

Figure 4. 2 Test Cube: Water phantom (blue) with three aluminum cubes (yellow) inside.

4.2.1. Energy degrader

As helium ions and protons at the same initial kinetic energy per nucleon have approximately the same range, no alteration to the detector design was required for the 200 MeV/u beam. For the remaining higher energies, it was necessary to add an energy degrader in between the rear tracker and the energy detector to account for the larger range. Subsequently, the degrader thickness was changed according to compensate the range difference between the respective higher beam energy and the 200 MeV/u case. Basing on the state of the art and on the degrader ideal requirements, the chosen material for the energy degrader was copper (with a RSP of 5.52). In relation to the copper degrader's thicknesses applied: for the 225 MeV/u, 250 MeV/u, 275 MeV/u, 300 MeV/u and 325 MeV/u cases thicknesses of 1.053 cm, 2.179 cm, 3.357 cm, 4.612 cm and 5.926 cm were used, respectively. These thicknesses values were the same both for the water cube and head phantom's simulations.

4.2.2. WET resolution of the pCT Scanner

The energy deposited in the final stage of the detector can be converted to the residual range of the proton R_i in the stopping stage. Recurring to the Bragg-Kleeman rule, the WET is:

$$WET = R_{tot}\text{-}S_0\text{-}S_1\text{-}S_2\text{-}\ldots\text{-}S_{i-1}\text{-}AE_i^p \qquad 4.\ 1$$

where R_{tot} is the integral over the inverse stopping power between zero and initial energy in the Continuous Slowdown Approximation (CSDA) of energy loss and S_i refers to the 5 stages' position[8]. The uncertainty in WET derives from range straggling of the particle in material, culminating to the final stage S_i together with the uncertainty associated to the particle's residual range in the final stage S_i together with the uncertainty in the particle's residual range in the final stage $R_i=\alpha E_i^p$,

$$\sigma_W \simeq \sqrt{(0.011.(Rtot - Ri))^2 + (p.Ri.\delta E)^2} \qquad 4.\ 2$$

where δE is the resolution of the measurement of the energy deposition in the final stage.

4.3. Wedge Calibration Simulation on TOPAS Simulation toolkit

The wedge calibration was performed according to the procedure used in Piersimoni, et al. (2017)[68] and Bashkirov, et al. (2016)[8]. The wedge calibration simulation has as main aim to convert the response of the Residual Energy/Range Detector (RERD) directly to Water Equivalent Thickness (WET). The detector measures scintillation light, which shows a non-linear relationship with the linear energy transfer (the stopping power). WET calibration is performed to take into account the tracker's WET, and the air between beam nozzle and the detector entrance. Furthermore, for different energies, the calibration also takes into account potential variations in the degrader size, in a way that a correct WET output for a given energy response in the stage is always obtained.

The wedge calibration simulation was performed in *TOPAS* simulation toolkit. The procedure consisted of 5 individual calibration runs. In the first run, data is taken with just the wedge phantom installed without the bricks. The wedge was defined setting its material as G4_Polystyerene and had a thickness of 50.8 mm, and a width of 209.5mm. To cover the full range of the WET that can be imaged with the 200 MeV/u' case, five removable polystyrene bricks of 50.8 mm thickness are added one-by-one in the four subsequent runs to the variable part of the phantom during the calibration. The same procedure has been used for all energies investigated. The calibration procedure is represented in *Figure 4. 3* taken from Dickmann et al. (2019)[25]. Therefore, WET was acquired from the 200 MeV-325 MeV/u helium ions' depth dose curves directly from the simulation. The lateral scatter was accounted for in the calibration procedure, where the path length through polystyerene was calculated using the income and outcome point coordinates of the particles. A straight line through the calibration phantom was estimated and translated to WET by multiplication of the straight line's length connection with the known RSP of the phantom. The WET values were acquired recurring to the RSP of the polystyerene (1.038)[68].

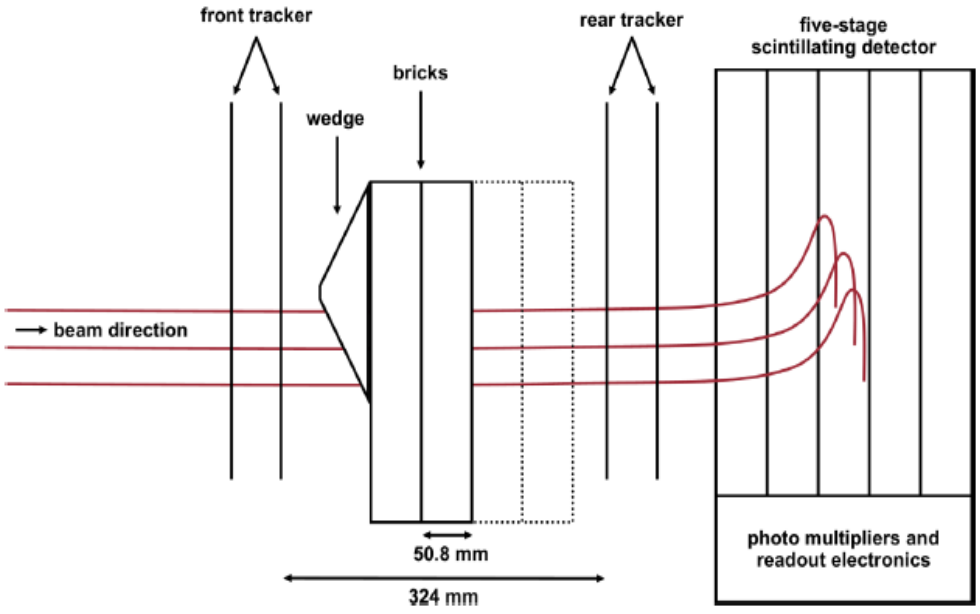

Figure 4. 3 pCT scanner with front and rear tracking and the five-stage detector. A wedge phantom is placed in front of two bricks and it is possible to add up to 4 bricks. Image taken from Dickmann et al. (2019)[25].

Each WET value was computed as the polystyerene lengths sum multiplied by their relative stopping powers. For each particle, the WET was related to the energy deposit to the stopping stage (the final stage in beam direction the particle reached into) and binned into a 2D WEPL versus energy histogram (1 mm bin size in WEPL 0-260mm range, 1 MeV bin size in energy and 0-340 MeV range). The calibration curves were found, by obtaining the most-likely (peak) WET value for each energy bin from the 2D histogram. The WET peak position was calculated as the arithmetic mean within the full width half maximum window around the maximum of the WET distribution. The calibration results in 5 calibration curves (one for each stage of the five stage MSS), relating the energy deposited by a particle stopping in the respective stage to the most likely WET it traversed. These five calibration curves, for 200 MeV/u irradiation energy, represented in *Figure 4. 4*, were used to convert the energy deposit for each particle history into WET values.

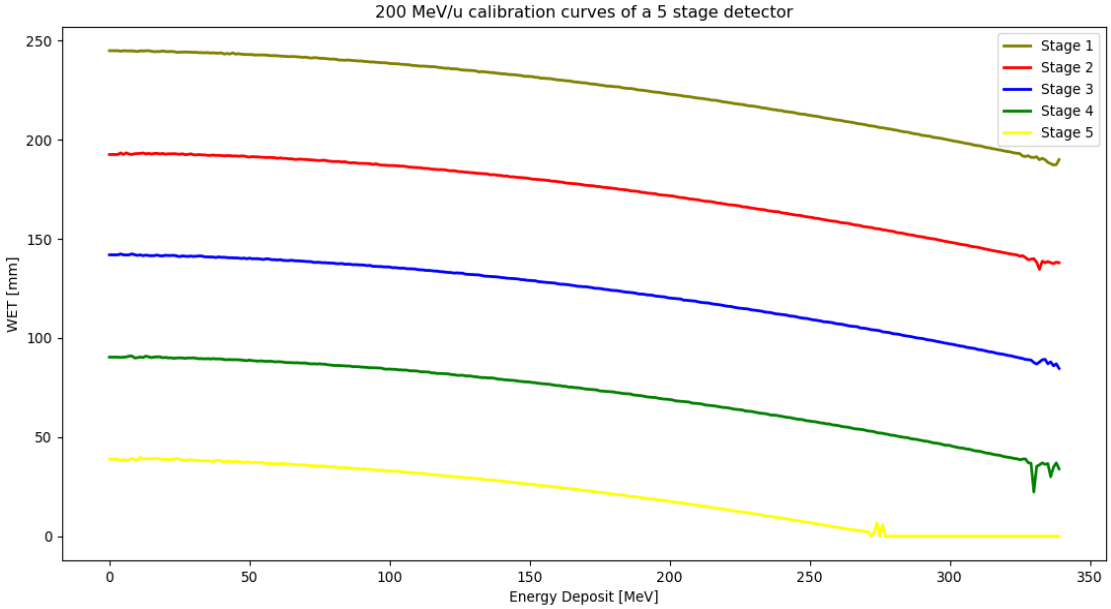

Figure 4. 4 200 MeV/u calibration curves of the 5 MSS detector using the wedge phantom.

4.4. Particle's Path simulation on TOPAS simulation toolkit with the Cubic Spline Path algorithm

To achieve a comparison between the particle's path simulation on TOPAS simulation toolkit and the one obtained using the Cubic Spline Path (CSP) formalism, an additional simulation was performed. The aim was to compare how accurate the path estimate was with respect to the actual path traced by the particles through the phantom.

The simulation performed involved the creation of a rectangular beam with 200 MeV/u of initial energy irradiating a water phantom box with 20 cm of thickness. This water phantom box, with the aluminum box inside it, was divided into multiple phase space scorers to record particles' important information along the water phantom such as position, direction, and energy. This way it was possible to infer the particle's path and to perform path reconstruction on TOPAS simulation toolkit.

Applying the Cubic Spline Path algorithm on *Python* and implementing it on this simulation, a trajectory of a particle along the phantom was obtained along the phantom's depth z in cm and it was

compared to the TOPAS simulation trajectory without applying any algorithm. This Cubic Spline Path implemented on the *python* script has been proposed by Collins-Fekete et al. (2015)[29] and it is explained in section 3.1.2 of the State of The Art. In *Figure 5. 1* of the Results section it is possible to visualize the comparison.

To compute the MLP accuracy for the different energies, the uncertainty matrix of the MLP formalism by Schulte et al. (2008)'s paper[81] (equation 3. 13 in section 3.1.1) was evaluated theoretically using the software written by Volz et al. for their 2020 work[89]. For that, a 5th order polynomial parameterization of the $1/(p(x)v(x))^2$ function was derived as in Schulte et al. (2008)'s work[81]. To obtain the parameterization, 100000 protons were simulated in water, recording their kinetic energy (E(x)) in steps of 0.5 mm. The kinetic energy was converted to the $1/(p(x)v(x))^2$ using the relationship:

$$1/(p(x)v(x))^2 = \frac{(E(x) + m_p c^2)^2}{(E(x) + 2m_p c^2)^2 E(x)^2} \qquad 4.\ 3$$

Where x is the depth in water, and m_p is the proton rest mass, c is the speed of light. The mean $1/(p(x)v(x))^2$ function for the particles was then fitted by a 5th order polynomial function, and the parameters of that fit had been used to compute the scattering matrix elements. This was finally inserted in the definition of the uncertainty matrix of the MLP (equation 3. 13), and the result was scaled by the ratio of the proton to the helium ions mass, in order to obtain the correct scattering displacement of helium ions (as shown in Gottschalk et al. (2012)'s work[37]). A plot of the Root Mean Square (RMS) error as a function of depth in water for the particle's histories analyzed can be seen in *Figure 5. 2* of the Results section.

4.5. Data filtering

Due to the fragmentation of the primary helium ions, both inside the object and inside the detector, it was necessary to use a △E-E filter to allow for identifying primary helium ions, and remove the fragment contamination in the recorded imaging data. The △E-E filter used in this thesis was based on the one from Volz, et al. (2019)'s study[93]. In addition, pre-calibration filters as outlined in Volz et al. (2019)'s study[93] were used. The pre-calibration filters involved in this thesis removed events which had a higher energy deposit than predicted by a single particle in the Bragg-peak stage. A minimum required energy deposit in each stage leading up to the stopping stage (threshold filter) also defined which events were removed. Finally, the 3σ WET filter was then applied within the image reconstructions: the particles were binned into 1 mm pixels based on their recorded position on the rear tracker into a 2D histogram from the ROOT data analysis framework, and for each histogram bin the WET and angular distribution standard deviation was calculated. Only those events were considered for image reconstruction for that the WET and angular displacement was within a ± 3σ region around of the bin mean.

The △E-E filter was obtained through the calibration simulation but with only electromagnetic interactions (as evidenced by the missing secondary particle lines in *Figure 5. 6* from the Results Section). It was also necessary, before the calibration to WET, to parametrize the primary helium curve with two 2nd order polynomials to restrain the filter to an adequate interval. Following, these parameters, which define the filter interval to the image reconstruction for both simulated phantoms, were implemented. The parameters were employed during image reconstruction.

The ΔE−E telescope measures the energy loss in an absorber, ΔE, and the total residual energy, E, in the absorber placed immediately next to the first one for each projectile travelling within the system. Following, the 5-stage energy detector was adapted to be used as a ΔE −E telescope. The energy deposit measured in the stage where the ion stops (Bragg-peak stage) was denoted as the residual energy E. ΔE was defined as the energy deposited for the same event in the stage right next to the Bragg-peak stage (denoted as ΔE stage). For each stage (except stage 1) the ΔE−E spectrum was plotted by employing the detector response from the 5 calibration runs. The ΔE − E filter consisted of comparing the relationship between the energy deposit in the Bragg-peak stage and the respective ΔE stage to the parameterization of the helium response curve. The events for which the ΔE − E relationship was not within the parameterized helium curve were excluded for the image reconstruction. The spectrum was obtained by plotting the energy loss associated to the Bragg-peak stage of all particles that stopped in that stage, versus their energy deposit in the ΔE stage. The obtained △E-E spectrum and its fitting curves and parameters are represented in *Figure 5. 6* in Results section.

4.6. Radiography reconstruction

As mentioned above, two different phantoms were used on this thesis, the pediatric head phantom and the test phantom. To reconstruct the images associated to both phantoms the radiography algorithm developed by Collins-Fekete et al. (2016)[19] was applied. This image reconstruction applied a maximum likelihood least radiography's square estimator.

To estimate the particles' path inside the phantoms an approach has been proposed by Collins-Fekete et al. (2015)[29] and this thesis applied the mentioned approach which consisted on the cubic splines' usage. This algorithm was written in *ROOT* using the method proposed by Collins-Fekete et al. (2015)[29] with the pixel size for the image reconstruction (set to 0.25mm for the test phantom and 0.5 mm for the head phantom).

4.7. Image Quality analysis

4.7.1. Spatial Resolution

Modulation Transfer Function (MTF) allows the characterization and quantification of an imaging system's performance in terms of spatial resolution. There are several methods associated to determine the MTF of an imaging system (edge, slit or point images). Usually, when the MTF is intended to be measured, a point source, corresponding to Point Spread Function (PSF), a slit, corresponding to a Line Spread Function (LSF),[17,60] and a knife edge, corresponding to Edge Spread Function (ESF) are imaged[22].

In this thesis, the assessment of the image spatial resolution was performed by deriving the MTF from the simulated test phantoms. The spatial resolution of these helium-beam radiographs was assessed by analyzing the three edges between the water and the aluminum cubes' inside the phantom. These straight edges later are fitted with an error function, which for particle imaging is the accurate fit function

due to the Gaussian form of the scattering[54]. The error function used to fit the ESF was defined by four parameters[32]:

$$ESF_{fit}(x)= a.\ erf\ (b(x-c)) +d \quad (4.4)$$

The ESF_{fit} was then numerically differentiated to obtain the LSF and finally, the following equation was used as the MTF[32]:

$$MTF= \frac{|\mathcal{F}\{LSF\}|}{|\mathcal{F}\{LSF\}|v=0|} \quad (4.5)$$

where $\mathcal{F}$ represents the discrete fourier transformation. The MTFs obtained for the test phantoms of this thesis are represented in section 5.4.2 of the Results. Spatial resolution is measured in this thesis by $MTF_{10\%}$, which can be defined as the spatial frequency (v) at which 10% of MTF(0) is attained[32].

4.7.2. Contrast-to-Noise Ratio (CNR)

In Gehrke, et al. (2018)[32] the image noise property was analyzed through Contrast-to-Noise Ratio (CNR) and evaluated against absorbed dose. The CNR can be defined as the ratio between the contrast and image noise:

$$CNR=\frac{|\langle S1\rangle-\langle S2\rangle|}{\sqrt{\sigma^2 S1+\sigma^2 S2}}, \quad (4.6)$$

where $\langle S_1\rangle$ and $\langle S_2\rangle$ are the mean WET values of two homogenous regions of interest (ROIs) in the helium ion radiography and σ_{S1} and σ_{S2} are the standard deviations of two homogenous ROIs. In this thesis, the CNR of the test phantoms was measured using ROIs in two homogeneous parts of the image, the water and the aluminum cubes, using the equation above. The CNR values obtained for the simulated test phantoms are represented in section 5.4.2 of the Results.

4.7.3. Per-pixel noise

In order to investigate the per-pixel noise of the reconstructed images for the head phantom, the standard error of the WET distribution in a pixel (standard deviation divided by the square root of the number of particles N recorded in that pixel) was investigated. This includes not only the straggling but also the scattering noise contributions. I.e. particles that crossed different regions in the head (bone and soft tissue) can end up in the same image pixel, broadening the pixel WET distribution. Consequently, when assessing the noise as function of the energy, it is important to look at heterogeneous objects as well. The recorded standard error per-pixel can be understood as the standard error of the WET distribution recorded given by[19]:

$$\aleph(\epsilon_k;0,\ \sigma^2_k)= \frac{1}{\sqrt{2\pi\sigma^2 k}} \exp\left\{-\left(\frac{\ell k,n}{\sqrt{2}\sigma kLn}\right)^2 (WEPLn - WETk)^2\right\} \quad 4.\ 7$$

where its components are explained in section 3.2.1.

4.8. Primary particles' loss count simulation on TOPAS simulation toolkit

In order to estimate how much more particles are necessary to compensate the primary particles' loss for higher beam initial energies, a large water box, with thickness equal to the range of a 325 MeV/u helium ion beam (58.63 cm), was simulated and irradiated with all of the energies previously used (200, 225, 250, 275, 300 and 325 MeV/u). The water phantom was divided into multiple Z bins which were set as phase space scorers to score the number of primary particles as function of the depth in the water phantom. This provides a primary particle's loss count profile for each of the energies used. The representation of this profile is on section 5.2. of Results.

5. Results

5.1. Particle's Path Estimation

A rectangular beam was simulated to irradiate a water phantom box. The water phantom was then divided into numerous phase space scorers allowing for path estimate with Monte Carlo simulation on TOPAS simulation toolkit. Following, the Cubic Spline Path algorithm was implemented on python to estimate the same path along the water phantom. This Cubic Spline Path implemented on the *python* script has been proposed by Collins-Fekete et al. (2015)[29]. A plot including these two path simulations with different methods is represented in *Figure 5. 1*. In this figure, the estimated particle path formalism, the optimized cubic spline path formalism, is overlaid onto the true particle trajectory from TOPAS simulation toolkit for a better understanding the path estimation concept.

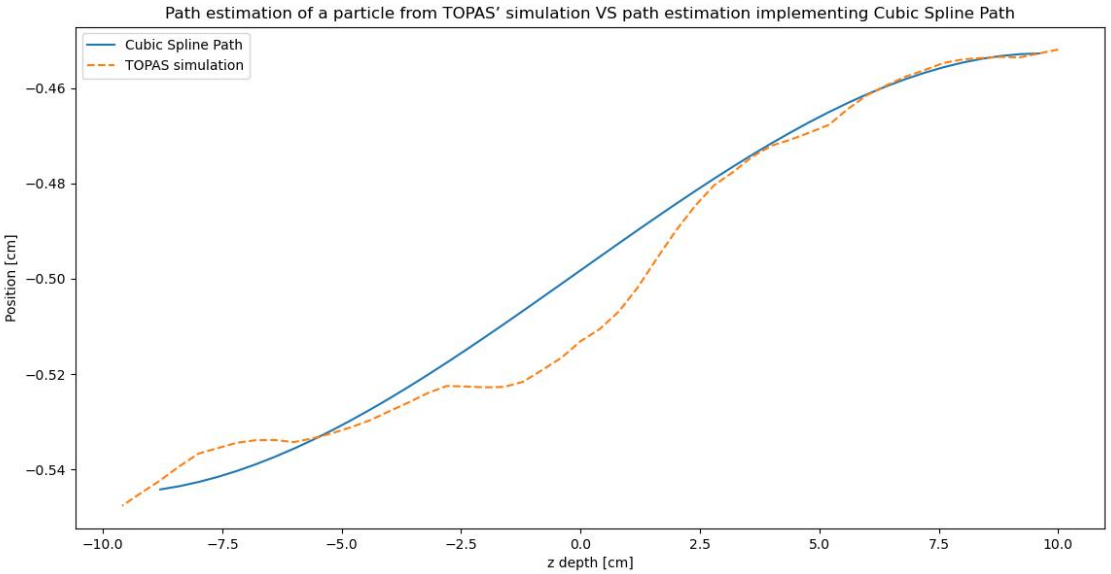

Figure 5. 1 Path estimation of a particle from TOPAS' simulation (Monte Carlo simulated trajectory) compared to the path estimation implementing the Cubic Spline Path algorithm.

Subsequently, the standard deviation of the most likely path was calculated as in Schulte, R. W., et al. (2008)'s paper[81]. The necessary parametrization of the $1/pv^2$ function was also obtained as in Schulte, R. W., et al. (2008)'s paper[81]. A plot of the Root Mean Square (RMS) error as a function of depth in water for the particle's histories analyzed can be seen in *Figure 5. 2*. The uncertainty of the path estimation is shown as calculated theoretically from the uncertainty matrix of the MLP. It can be seen that with increasing initial energy, the maximum uncertainty of the path estimation increases. Since the path estimation precision is directly linked to the spatial resolution, this also indicates an increase in spatial resolution. However, it can also be seen, that while the initial increase in path estimation precision is significant, this is not linear with increasing energy, such that the path estimation increase in accuracy is little for the highest energies investigated.

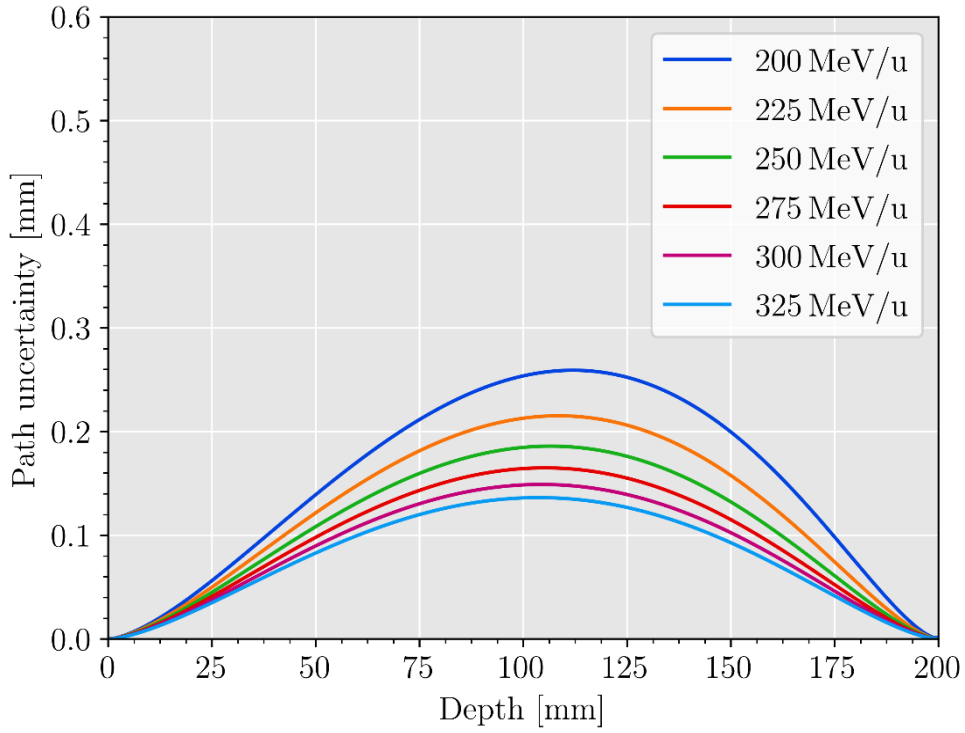

Figure 5. 2 Standard deviation of the most likely path estimation, representing the Root Mean Square (RMS) difference, for each irradiation energy, calculated theoretically from the uncertainty of the MLP as given in Schulte et al. (2008)'s work[81].

5.2. Primary Particle's Loss

A water box of 58.65 cm of thickness was simulated and irradiated with 200 MeV/u-325 MeV/u beam energies. The water box was subsequently divided into multiple Z bins to score the number of particles that stop along the water box's depth. In *Figure 5. 3* is represented this primary particles' loss profile. It is possible to observe that for lower energies, the sharp drops are placed at a lower depth, evidencing a lower range reached by the particles. In addition, a higher loss of primary particles occurs for higher energy values.

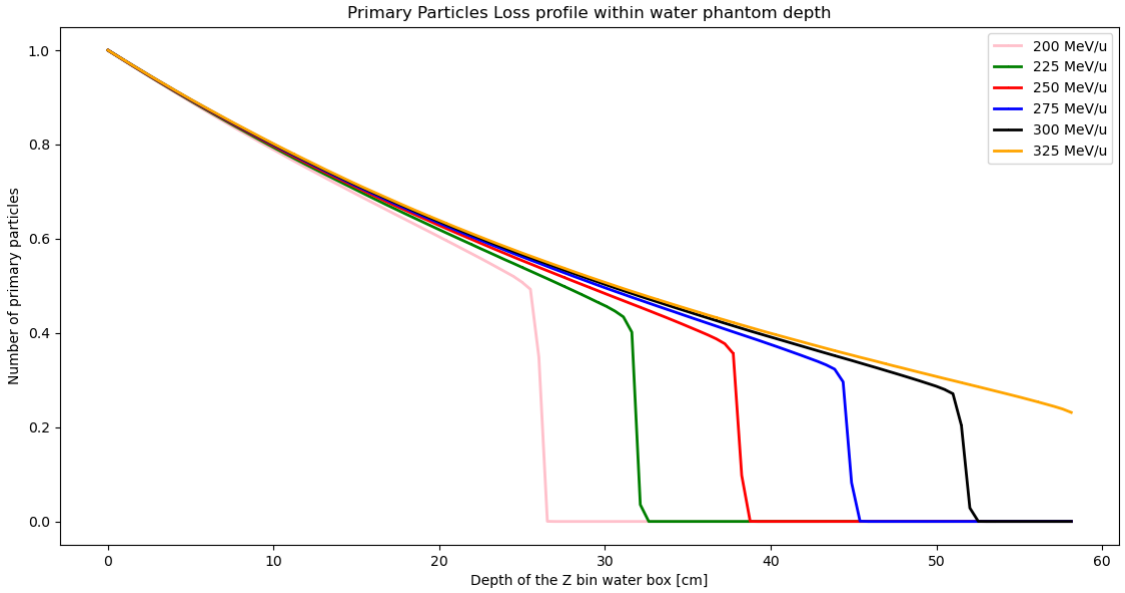

Figure 5. 3 Primary particles' loss profile within the water phantom's depth for each beam energy.

The data related to the previous figure allowed for the relative primary particles' loss calculation with the initial number of particles and the number of particles right before the sharp drop. This is represented in *Figure 5. 4*. As represented, the relative primary particles loss in % increases with increasing energy as mentioned and represented above as well. For energies above 320 MeV/u, there is an approximate 77% relative primary particles loss.

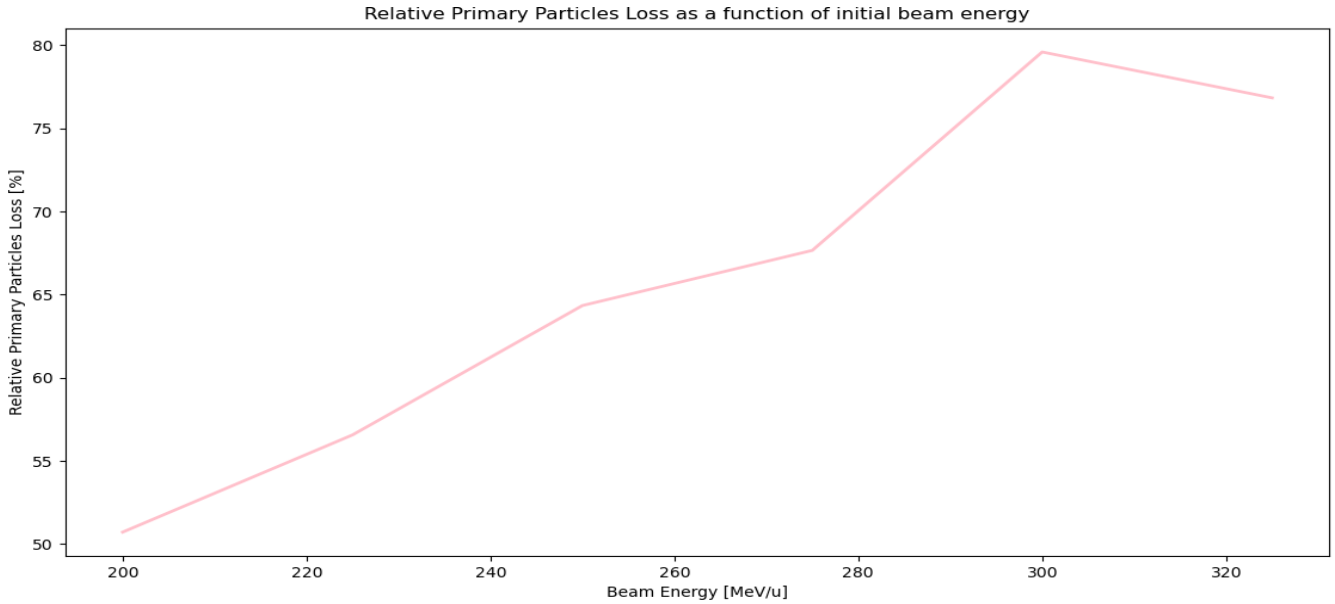

Figure 5. 4 Relative primary particles' loss as a function of initial beam energy.

5.3. Phantoms' reconstructions

5.3.1. Head Phantoms

In relation to the reconstructions without the ΔE-E filter: in *Figure 5. 5* is represented the pediatric head phantom reconstruction, based on a X-ray CT scan provided by Giacometti et al. (2017)[34]. The phantom was simulated with a 200 MeV/u beam and 10 000 000 particles without the application of the ΔE-E filter and without the degrader's presence since it was not necessary. The reconstruction without the application of the ΔE-E filter was only tested for one energy value, the 200 MeV/u beam energy. The head phantom reconstruction displays a noisy blurred image due to the inclusion of the secondary fragments (without ΔE-E filter). These fragments produce noise and a reduction of the spatial resolution. It is possible to observe equal behavior of the image reconstructions from Gehrke et al. (2018)[32].

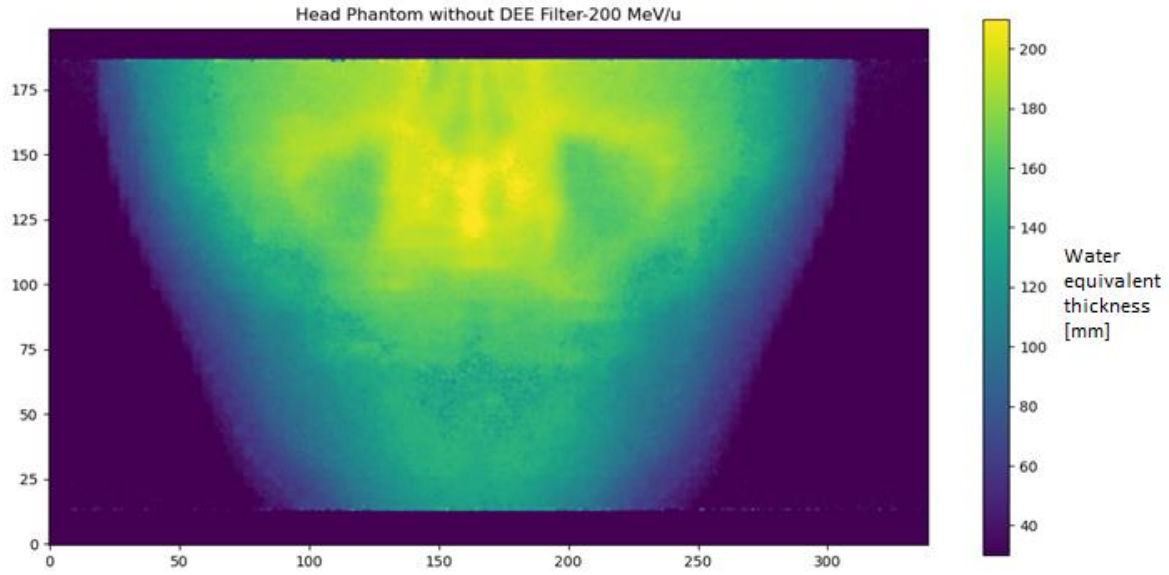

Figure 5. 5 Pediatric head phantom reconstruction without ΔE-E filter applied, without degrader and irradiated with a 200 MeV/u beam and 10 000 000 particles.

For the reconstructions using the ΔE-E filter, in *Figure 5. 6* was acquired for a simulation without nuclear interactions (only the physics model g4em-standard_opt4 activated) in order to have only primary helium ions for better a parameterization. *Figure 5. 6* represents the helium curve of the ΔE-E filter fitted with two 2nd order polynomials:

$$\Delta E_{low} = 0.000944E^2\text{-}0.810072E\text{+}310.690580 \quad (5.1)$$

and

$$\Delta E_{high} = 0.000944E^2\text{-}0.810072E\text{+}325.190584. \quad (5.2)$$

where E is the energy deposit in the stopping stage. These fitting parameters were constant for the remaining head and water cube phantom's simulations for all energies since the ΔE-E filter is not sensible to energy changes.

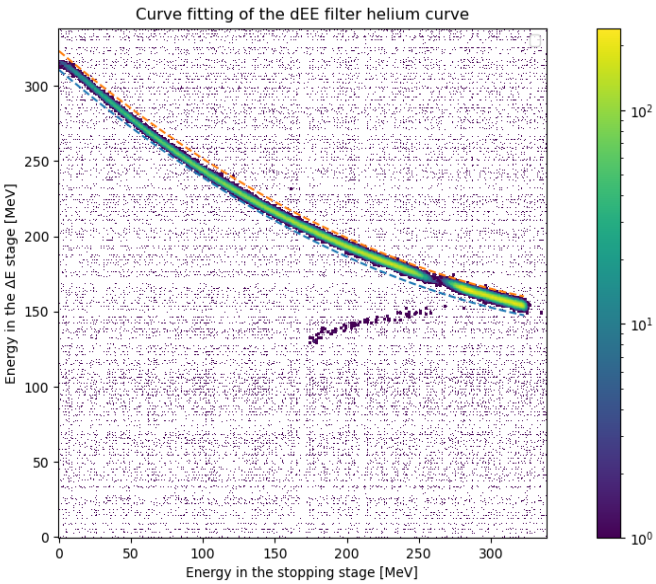

Figure 5. 6 Helium curve in the ΔE-E filter with two 2nd order polynomials fitting. This plot was acquired for a simulation without nuclear interaction (i.e. only helium ions scored) to define the filter parameters.

In *Figure 5. 7 a)* is represented the pediatric head phantom reconstruction. The phantom was simulated with a 200 MeV/u beam and 10 000 000 particles with the application of the ΔE-E filter and without the degrader's presence since it was not necessary.

The remaining figures *(Figure 5. 7 b)-f)*) represent the head phantoms reconstructions simulated with 225-325 MeV/u beam energies with 10 000 000 particles and ΔE-E filter as well. The only difference with the 200 MeV/u beam case resides on the degrader application on the pCT scanner for each of these energies.

With the application of the ΔE-E filter it is possible to observe qualitatively a great decrease in noise and blur on the image reconstructions. In addition, the spatial resolution increases for higher beam energies, as qualitatively seen with the better visibility of the fine facial structures of the head phantom.

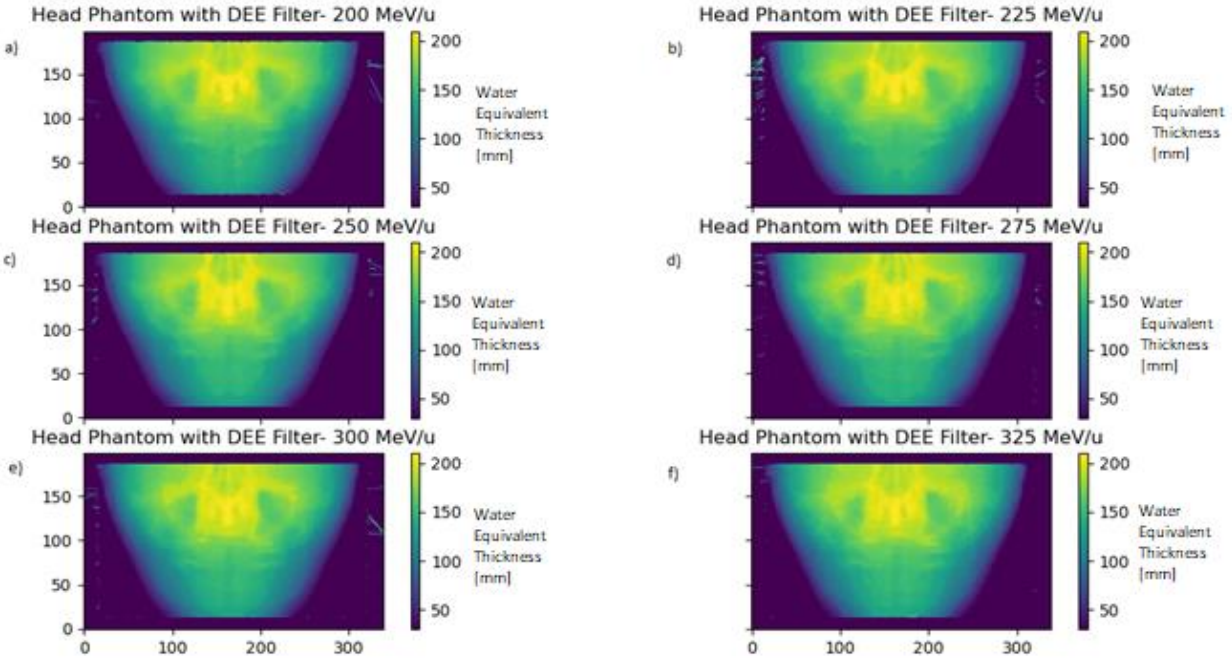

Figure 5. 7 Head phantom reconstructions with ΔE-E filter applied and irradiated with 10 000 000 particles. a) Using a 200 MeV/u beam energy without energy degrader; b) to f) Using energies from 225 MeV/u to 325 MeV/u, respectively, with the addition of a degrader for each case.

5.3.2. Test Phantoms

In relation to the reconstructions without the ΔE-E filter: in *Figure 5. 8* is represented a reconstruction of an 80 mm width water cube with three 10 mm width aluminum cubes inside. The phantom was simulated with a 200 MeV/u beam with 10 000 000 particles and without ΔE-E filter and degrader.

The test phantom reconstruction displays a noisy blurred image due to the inclusion of the secondary fragments (without ΔE-E filter). These fragments produce noise and a reduction of the spatial resolution. It is possible to observe equal behavior of the image reconstructions from Gehrke et al. (2018)[32].

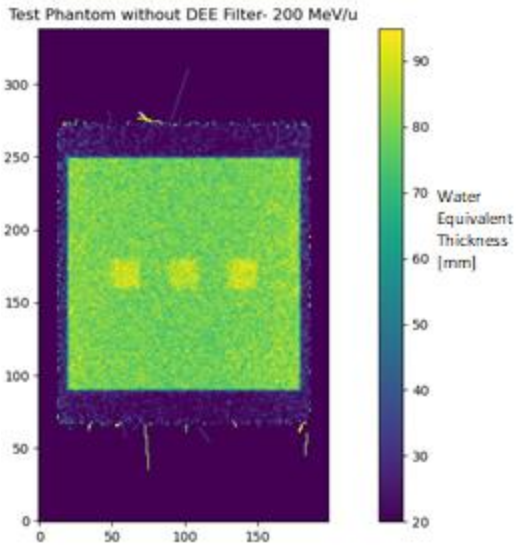

Figure 5. 8 Water cube reconstruction with aluminum cubes inside without ΔE-E filter applied, without degrader and irradiated with a 200 MeV/u beam and 10 000 000 particles.

For the reconstructions with the ΔE-E filter: in *Figure 5. 9 a) i*s represented the water phantom reconstruction. The phantom was simulated with a 200 MeV/u beam and 10 000 000 particles with the application of the ΔE-E filter and without the degrader.

The remaining figures (*Figure 5. 9* b) to f)) represent the water phantoms reconstructions simulated with 225-325 MeV/u beam energies with 10 000 000 particles and ΔE-E filter as well. The only difference with the 200 MeV/u beam case resides on the degrader application on the pCT scanner for each of these energies.

With the application of the ΔE-E filter it is possible to observe qualitatively a great decrease in noise and blur on the image reconstructions. In addition, the spatial resolution increases for higher beam energies, as qualitatively seen with the better visibility of the three aluminum cube's edges.

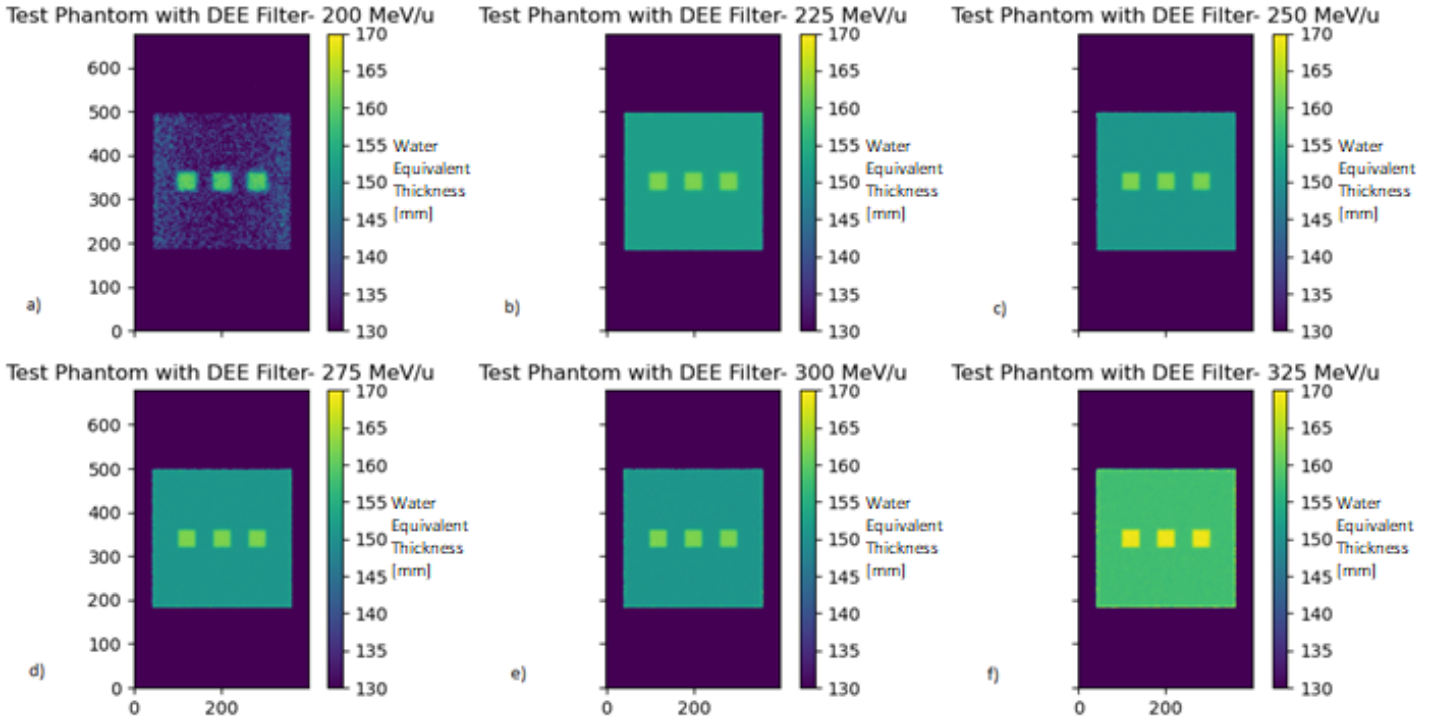

Figure 5. 9 Test phantom reconstructions (water cube with 3 aluminum cubes inside) with ΔE-E filter applied and irradiated with 10 000 000 particles. a) Using a 200 MeV/u beam energy without energy degrader; b) to f) Using energies from 225 MeV/u to 325 MeV/u, respectively, with the addition of a degrader for each case.

5.4. Image Quality analysis

5.4.1. Head Phantom

Noise is defined as the standard deviation of the WET distribution in a pixel divided by the square root of the number of particles N recorded in that pixel. This value was extracted using in function of the *ROOT* 2D histograms, which were used to store the image data. The noise map was only applied for the head phantoms with the ΔE-E filter. *Figure 5. 10* from *a)* to *f)* represent the dose maps acquired for all of the energy's range used.

The lines in the images likely correspond to the increased noise at stage interfaces of the 5-stage scintillator detector used. Particles stopping in the reflective foils between the stages, or with an energy deposit lower than the 1 MeV stage threshold, will get assign the previous stage in upstream direction as stopping stage, which then results in a systematically too high WET being calculated for these particles[7]. This results at significantly more noise at stage interfaces. Interestingly, this seems to increase with increasing energy. On the other hand, the noise corresponding to heterogeneities in the head phantom visibly decreases with increasing energy.

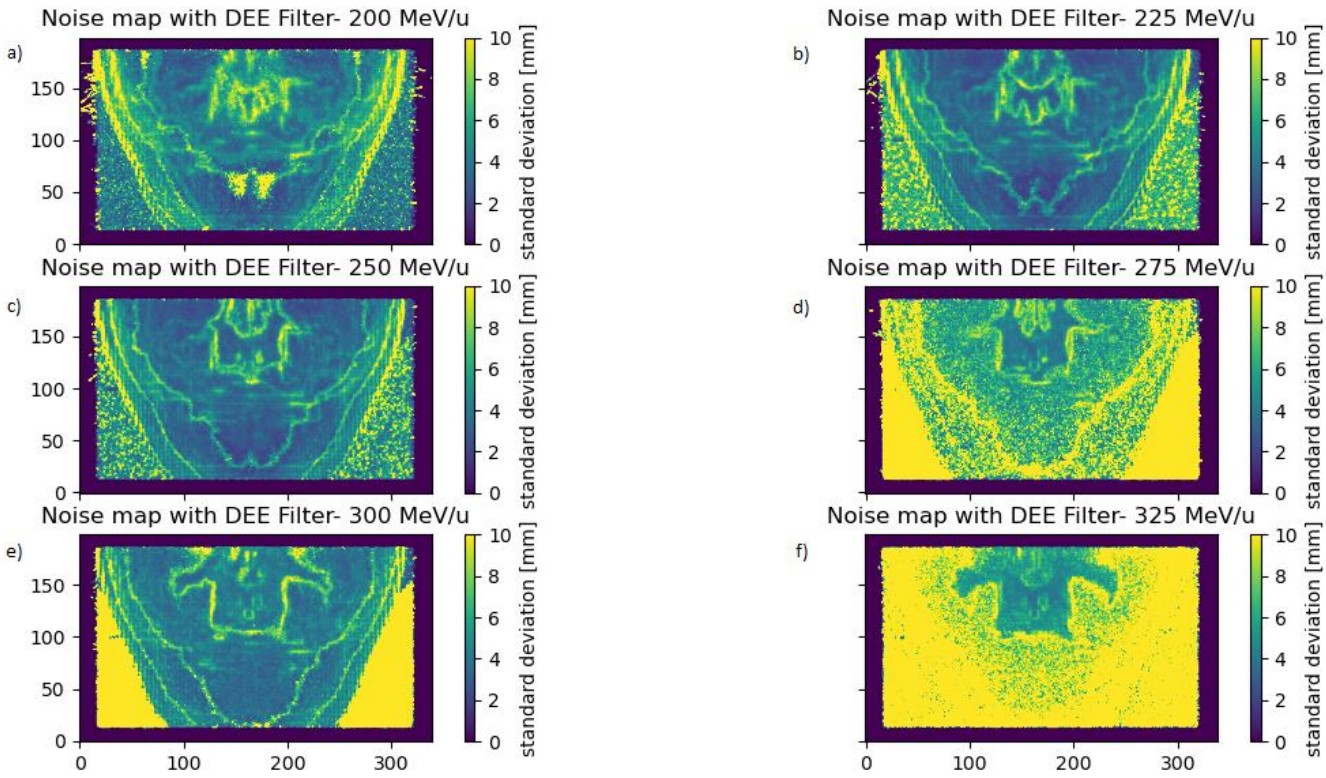

Figure 5. 10 Noise maps for the head phantom with ΔE-E filter applied and irradiated with 10 000 000 particles. a) Using a 200 MeV/u beam energy without energy degrader; b) to f) Using energies from 225 MeV/u to 325 MeV/u, respectively, with the addition of a degrader for each case.

For the dose deposit calculation, a box was simulated with the same dimensions as the head phantom and set as volume scorer to score the dose deposit on that volume in μGy units. The dose deposit was only calculated for the head phantoms with the ΔE-E filter. The dose values acquired for each energy are represented in *Table 5. 1*.

Table 5. 1 Dose deposit values for each irradiated beam energy.

Beam Energy [MeV/u]						
	200	225	250	275	300	325
Dose Deposit [μGy]	84.47	76.60	70.95	66.61	63.11	60.26

5.4.2. Test Phantom

The image quality assessment was achieved using the MTF, applied in the simulated test phantoms. The spatial resolution was assessed by analyzing the edge of the middle cube inside the phantom. The MTF curves for all energies are represented in *Figure 5. 11*.

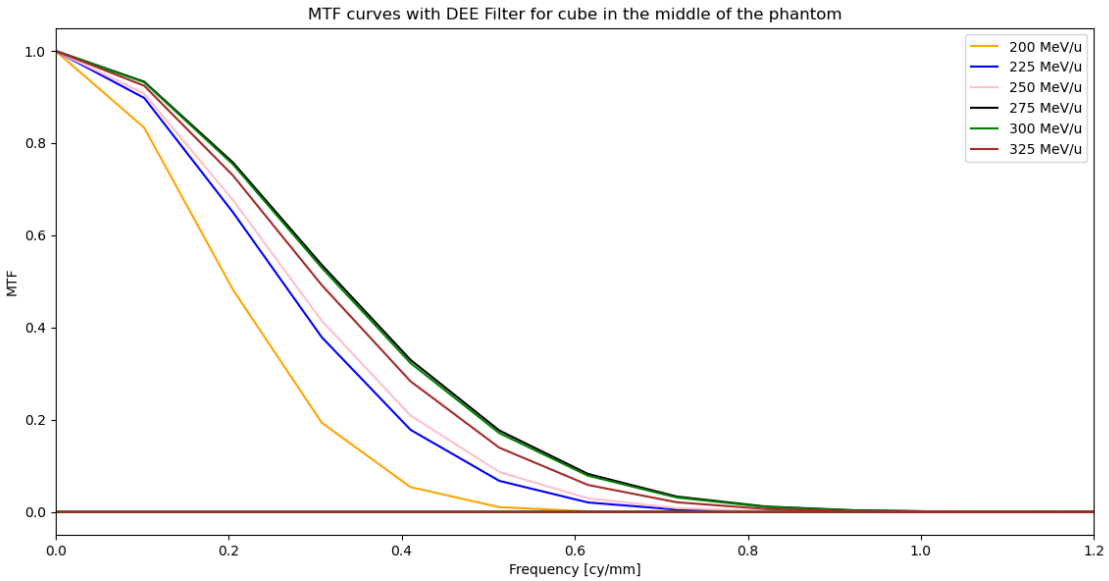

Figure 5. 11 MTF curves for the cube in the middle of the test phantom as a function of beam energy (from 200 MeV/u to 325 MeV/u).

It can be observed an improvement of the MTF values translating into a spatial resolution improvement. The 325 MeV/u case does not fit with the trend for the other MTF curves. The CNR can be defined as the ratio between the contrast and image noise where the means of two ROIs and its standard deviations are employed. The CNR of the test phantoms was measured using ROIs in two homogeneous parts of the image, the water and the aluminum part, as it is represented by the black squares on *Figure 5. 12*. The CNR values acquired for each irradiated beam energy are represented in *Table 5. 2*. From 225 MeV/u- 325 MeV/u there is a decrease in the CNR values that comes from both the increased range straggling and the increased loss of primary particles.

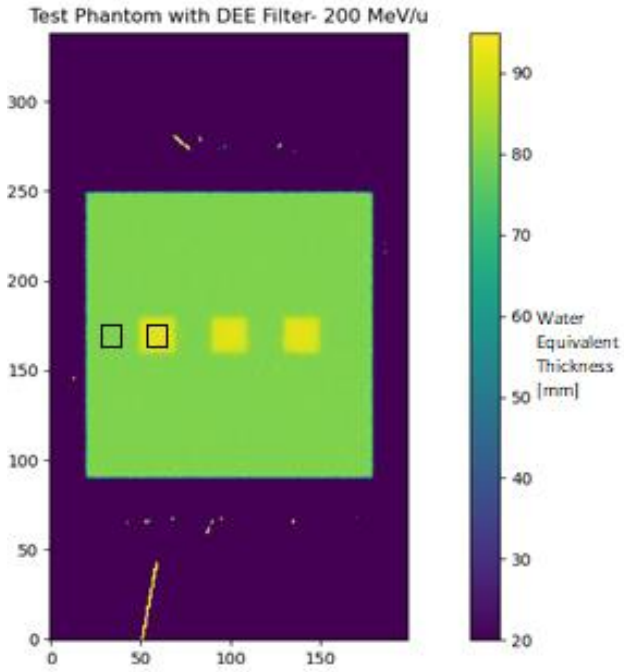

Figure 5. 12 ROIs, represented as the 2 black squares, used for the CNR calculation on the test phantoms. Example on the test phantom with the ΔE-E filter with a 200 MeV/u beam energy.

Table 5. 2 CNR values for each irradiated beam energy.

Beam Energy [MeV/u]							
	200		225	250	275	300	325
	Without ΔE-E filter	With ΔE-E filter	With ΔE-E filter				
CNR Value	1.61	2.45	15.96	15.16	13.37	12.10	9.25

6. Discussion

6.1. Particle's Path Estimation

Particle path estimation algorithms, such as the CSP, are used for improving the spatial resolution in particle radiography and pCT. The optimized CSP was used to estimate the particle trajectory and the subsequent optimization was Collins-Fekete et al. (2017)'s work[21].

Within higher beam energies, the particles suffer less from scattering due to their lower energy loss in the object. This leads to an increased path estimation accuracy, subsequently, leading to a better spatial resolution for particle radiography[29] as seen in *Figure 5. 2*, which represents the theoretical calculation of the path estimation accuracy. However, the path estimation accuracy increase is not directly proportional with the energy increase, but rather, the spatial resolution improvement is larger for the first energy steps and then saturates for higher beam energies. The MTF curves representing the spatial resolution improvement are represented in *Figure 5. 11* in the Results section. Similar results using the CSP are also found in Fekete, C. A. C, et al. (2015)'s study[29].

Moreover, as it is possible to observe in *Figure 5. 1* from the Results section, in the beginning and end of the particle's trajectory both curves intersect due to a front and rear tracker presence in the phantom whose record the particle's accurate position without any estimation. Furthermore, there is little difference between both trajectories which implies that the Cubic Spline Path Algorithm is a liable path estimation method as observed in *Figure 5. 2.* In this figure the maximum deviation of the path uncertainty for 200-325 MeV/u corresponds to approximately 0.26 mm, 0.22 mm, 0.185 mm, 0.165 mm, 0.16 mm, and 0.14 mm, respectively.

6.2. △E-E filter

Since data filtering is crucial for an accurate RSP reconstruction in particle CT, in this thesis, as mentioned before, 3 σ WET and △E-E filter were both applied before image reconstructions.

The △E-E filter had demonstrated to efficiently remove the systematic fluctuations, i.e. the secondary particles, and, subsequently, the RSP accuracy resembled the simulation without nuclear interactions involved. Thus, the 3 σ WET filter successfully removed the uncertainties associated to the energy detector, leading to an improved accuracy associated to the △E-E filter for helium radiography. The presence of secondary particle contamination broadens the WET distribution recorded in each image pixel reducing the 3 σ efficiency.

Independently of the initial energy, the relationship between the energy deposit in the final stage where the particle reached and the previous stage is fixed through the properties of the stoping power, and not dependent on the initial energy of the particle.Therefore, the △E-E filter is only detector specific: it depends only on the thickness and RSP of the detector stages. Consequently, the same 2nd order polynomial parameters used to restrain the filter to an adequate interval will be adequate to for any initial beam energy implemented.

6.3. Energy Degrader

In this investigation, higher beam energies are exploited in terms of resulting imaging quality in particle imaging. This energy increase leads to a greater image noise due to higher range straggling and WET resolution due to a deeper position associated to the Bragg peak with higher energies. In this thesis, basing on Amato, Martisikova and Gehrke, (2020)'s work[5], an energy degrader was added in between the rear tracker and the energy detector. Using this method, the energy degrader's thickness has to increase with the increasing of the beam energy to guarantee that the Bragg peak is fully contained within the detector limits.

The 5 stage energy detector of the US pCT collaboration prototype has a dynamic WET range (i.e. the range of WET it can image) of 260 mm. Meaning, for the higher beam energies investigated, particles crossing air or only a low WET value through the patient would fully cross the detector, providing no information (the detector requires the particles to stop within to infer the WET the travelled). In principle, one could think of simply using a larger detector (adding more stages), however, that would be impractical for clinical use. Thereofore, the use of a degrader is mandatory. The degrader was chosen in a way that the residual range of the particles inside the energy detector is comparable to the case of the 200 MeV/u beam for better comparison.

Five materials for the energy degrader were considered: aluminum, copper, tin, tungsten, and water. Water, tin, and aluminum were excluded due to their low RSP value, leading to a higher thickness needed to compensate higher energies. The goal was to choose a material which had a high RSP value to ensure the lowest thickness required to add to the detector. Tungsten has a higher RSP value than copper, although, due to its cost, copper was the choosen candidate to the energy degrader with a RSP of 5.52 from NIST data. Though, copper material is less ideal for nuclear interactions due to its high atomic mass, however, copper was chosen to be consistent with the work by Amato, Martisikova and Gehrke, (2020)[5].

6.4. Calibration

The wedge calibration on this thesis was performed as a method to establish a direct relationship between the Residual Energy Range Detector response (energy deposit in the stopping stage) and WET values. The WET values were obtained from the thickness the particles travelled through the calibration phantom scaled by the phantoms RSP. The thickness traversed was estimated based on the distance between the particle's entrance into the calibration phantom and its exit point, computed from the tracking detector measurements. The accuracy of the calibration sets the accuracy of the image reconstructions, therefore, a correct calibration is of integral importance.

In theory, for the simulations it would be possible to resort to the same 200 MeV/u calibration curves for all of the energies used (225-325 MeV/u) due to the energy degrader addition. For this reason, the degrader thickness was chosen such that it compensates for the difference between the initial range for the higher beam energy and that for the 200MeV/u case. In that way, for any WET crossed by the particles, their residual energy at the entrance of the energy detector would be approximately the same for all initial energies investigated. Consequently, also the energy deposit in the energy/range detector (and especially the stopping stage) would be the same (except for the increased range straggling broadening the distribution of energy deposit for a given WET). Consequently, since the calibration curves involve the link between the most likely WET and the energy in the stopping stage of the detector,

the energy in the stopping stage, maintained unaltered, it would be possible to always use the same 200 MeV/u calibration curves. The main aim of this approach would be to privilege simplicity in the investigation. *Figure 6. 1* represents a scheme of the approach explained regarding the same 200 MeV/u calibration curves' usage for all energies.

However, in practice, this is infeasible since it would require to precisely set the degrader WET exactly to compensate the difference between the initial beam range for the 200 MeV case and the higher energy cases. Hence, for this thesis, a set of calibration curves was simulated for each energy irradiation.

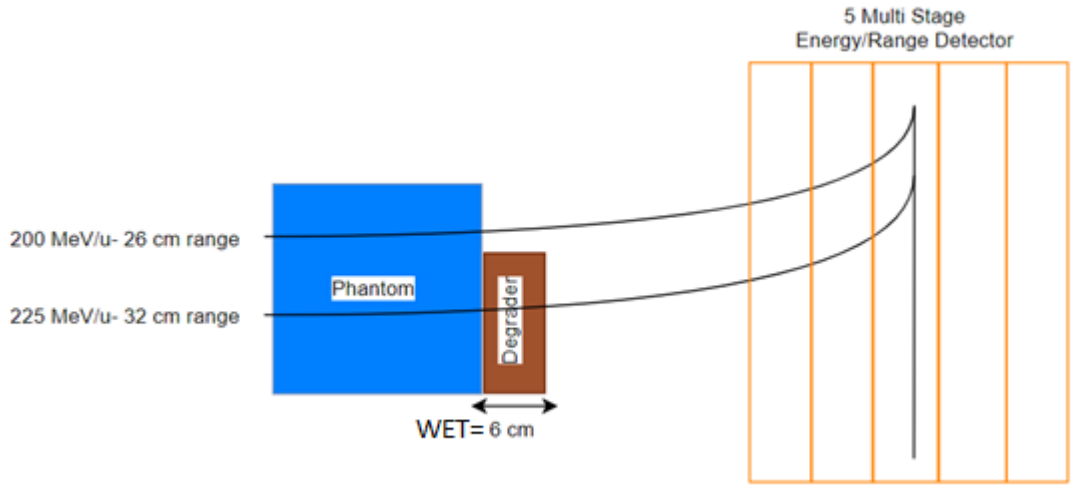

Figure 6. 1 Schematic representation of the energy degrader's role in positioning the Bragg peaks within the MSS in the same stopping stage.

6.5. Spatial Resolution

In relation to the path estimation applied in this thesis, it gives a good introduction to the improvement of the spatial resolution for the cube phantoms, the test phantoms. For this thesis, only the middle aluminum cube's MTF curves were displayed. This can be justified from the path estimation accuracy which is the worst in the middle part of the phantom. For the higher energies' case, owing to the CSP implementation, an improvement of the MTF values is observed which translate into a spatial resolution improvement as it is possible to observe in *Figure 5. 11*. The 325 MeV/u case does not fit with the trend for the other MTF curves and the reason for that reduced MTF for this case is likely due to the increased noise in the image. In terms of image reconstruction's observation of the test phantoms, with increasing energy it is clear that the spatial resolution improves looking into the aluminum edges. From energy to energy the spatial resolution improvement is highly noticeable and even more when comparing with beam energy values that are distant from one another.

Qualitatively analyzing the head phantoms' image reconstructions, an improvement of the spatial resolution of the fine structures in the face is observable with higher beam energies. This leads to an important question: do the image reconstructions need that much spatial resolution? The ideal scenario would be to optimize all the parameters involved to find a good balance between spatial resolution, beam energy, dose deposit, detector design and CNR. For instance, a higher irradiation energy improves the HU and RSP relationship optimization if an x-ray CT and particle radiographs are

combined[18]. However, Krah et al. (2018)[54] demonstrates that particle CT only needs 3 lp/cm to be useful for treatment planning.

6.6. Noise

The absolute image noise level depends on the heterogeneity of the phantom and is driven by MCS along the heterogeneities. The scattering contribution to noise is negligible in the center of a homogeneous phantom however, it becomes a leading source of noise around heterogeneities for an anthropomorphic head phantom. This fact is the lead reason why the per-pixel noise was only analyzed for the head phantom case on this thesis. This heterogeneous phantom's noise study is relevant since it has no precedents, and it is clinically relevant. The noise maps acquired for the head phantoms of this investigation are represented in *Figure 5. 10* of the Results section.

The noise is calculated as standard deviation of the WET distribution in a pixel divided by the square root of the number of particles N recorded in that pixel. I.e. the noise goes with 1/sqrt(N) meaning for less surviving helium ions more noise is present in the image reconstruction. This provides the information regarding the amount of extra particles needed to get the same noise. Therefore, a larger number of particles implies a lower noise level.

For higher energies, important points need to be considered: the higher energies, associated to higher ranges, will result in a broader range straggling (the range straggling for helium ions is roughly 0.0055*Range), increasing the noise[5]. Furthermore, since range can be described as Range = aE^p (Bragg Kleemann rule), the range straggling is a power function of the initial energy where $p \approx 1.74$ for helium ions in water[8].

In addition, a higher energy will result in a greater loss of primary particles due to more fragmentation, therefore, the number of particles reduces. This occurrence can be inferred from the ratio between the original and final (just before the fluence drop at the end of the particles' range) number of primary particles. This will lead to an increase in noise at the same number of primary particles. The visual representation of the initial and final number of primary particles can be observed in *Figure 5. 3* from the Results.

However, the Multiple Coulomb Scattering of the particles will decrease (due to the higher energy), which will lead to a lower noise close to large WET gradients (i.e. the facial structures). This is the reason why a head phantom is used, especially due to the facial structures where the scattering is expected to have a major effect on the noise.

In relation to the results regarding noise analysis of the head phantom: an increasing energy provokes more noise at stage interfaces. On the other hand, the noise corresponding to heterogeneities in the head phantom, i.e. facial structures, visibly decreases with increasing energy. The 300MeV/u case does not fit with the trend for the other phantoms and the reason for that at the time of writing is unknown.

6.7. Dose

One aspect of importance is the analysis of dose given to the patient, i.e. to the head phantom. *Figure 6. 2* is a representation of the dose given per primary particle for different beam energies. The increase of energy results in a reduced dose due to the $1/\beta^2$ dependence of the stopping power (from the Bethe formula). However, the increased loss of primary particles also means an increased dose per useful particle, i.e. particle used for image reconstruction. Therefore, even if more primary particles are needed to get to the same number of particles used for image reconstruction, these particles will give less dose. Hence, at the same dose, it is possible to use more primary particles at higher beam energies than lower beam energies[25]. This has also been discussed in Collins-Fekete, C. A, et al. (2020)' work[20].

By observing *Figure 6. 2* it is possible to conclude that the 300 MeV/u case has approximately twice the range as for the 200 MeV/u case which means that it also has approximately twice the range straggling. From *Figure 5. 3,* it is also possible to conclude that the amount of particles' loss for the 300 MeV/u case is also twice higher than for the 200 MeV/ case which allows to infer that, in order to get the same image noise (i.e. to be able to compensate the increased range straggling and loss of primary particles associated), four times more primary particles, approximately, are necessary. In addition, from observation of *Figure 6. 2*, an approximate factor of $\frac{6}{8.5}$ less dose is obtained per primary particle, therefore, this requires the need to use twice the amount of particles. Meaning, in order to obtain the same image noise, a $4\times\frac{6}{8.5}$ factor of more dose for the 300 MeV/u case is required in comparison to the 200 MeV/u case. Since this aspect is not compensated by MCS noise decrease, it is possible to conclude that the use of higher beam energies is not ideal.

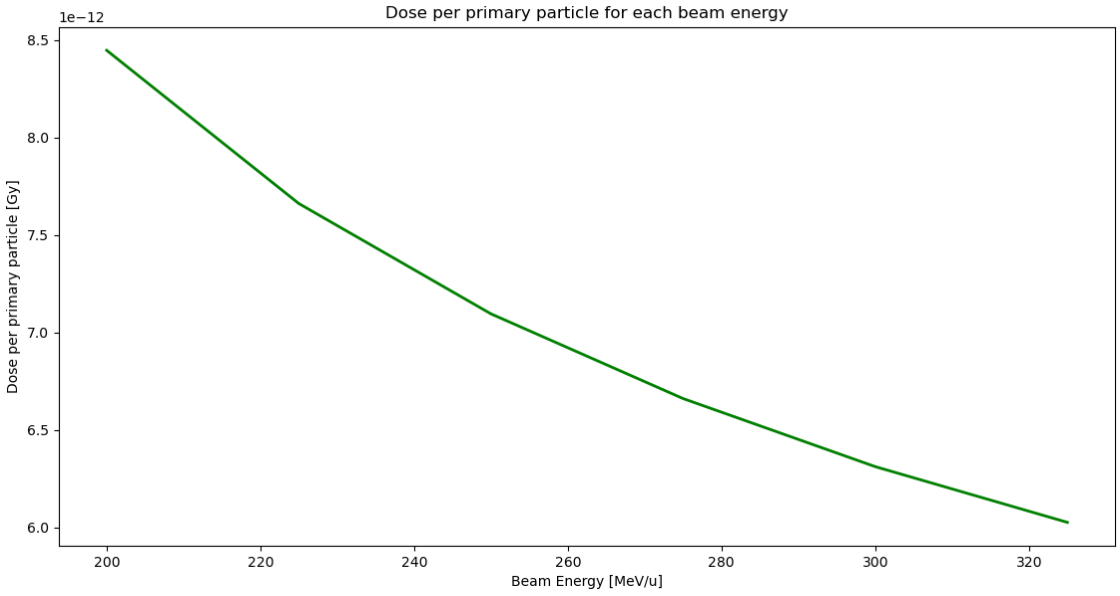

Figure 6. 2 Dose deposit per primary particle for each beam energy simulated. 10 Million primary particles were used for all simulations.

6.8. Energy/Range Detector improvements

The most striking issue related to noise is the loss of primary particles with higher beam energies resulting in an increase excess dose to the patient at the same noise level[20]. The current energy detector design performs quite well with increasing energy, with a WET resolution close to the straggling of the particles[90]. Although, the best improvement would be to not use a detector that requires the particles to stop within the detector. Specifically, with higher beam energies, the particles traverse a majority of their path in the detector rather than in the patient, meaning most of the primary particles useful for image reconstruction will also be lost inside the detector due to nuclear interactions.

The next improvement in terms of the detector would be using a Time-Of-Flight (TOF) detector[99], which does not require the particles to stop within the detector, meaning only the loss of primary particles and straggling inside the phantom are relevant. This detector measures the particle's residual energy from the time taken by particles traversing a certain distance (i.e. enables to infer the velocity), more specifically, between two detector planes acting both as RERD and rear tracker. Moreover, the relevant noise component corresponds to the time resolution of each detector panel.

However, the TOF detector has a high intrinsic noise of the detector associated due to the small variation of particle's velocity with higher energies. In addition, the TOF detector is unfavorable at high initial energies because it requires a high time resolution of the TOF planes[90]. In terms of TOF detector size when compared to the rear components of the pCT scanner prototype used for this thesis, to accomplish a WET resolution equivalent to the helium ions' range straggling, the time resolution of the detector planes would have to be better than 10 ps and even better for higher beam energies.

7. Conclusion

In this thesis, an investigation to improve the spatial resolution of helium-beam radiography was made basing on Amato, Martisikova and Gehrke, (2020)'s work[5]. Two different phantoms were simulated with *TOPAS* Simulation toolkit: a test phantom that consisted of a 15 cm width water phantom with three 1 cm width aluminum cubes inside and an anthropomorphic pediatric head phantom, based on a X-ray CT scan provided by Giacometti et al. (2017)'s work[34]. The noise contribution becomes highly visible around heterogeneities for an anthropomorphic head phantom justifying studying the per-pixel noise only for the head phantom case. This heterogeneous phantom's noise study has never been done previously and it has a high relevance for field or particle imaging.

A wide range of beam energies from 200 MeV/u to 325 MeV/u was used to irradiate both phantoms in the simulations. To compensate for the increasing range of particles, associated to the increasing energies, an energy degrader was added in between the rear tracker and the energy/range detector of the pCT scanner. The spatial resolution when analyzed as function of beam energy presents a rising behavior of approximately 46% from 200 MeV/u to 300 MeV/u. The 325 MeV/u is not included in this trend of the MTF curves possibly due to the increased noise in the image. A total CNR decrease of approximately 42% was measured for radiographs from energy 225 to 325 MeV/u.

In conclusion, while higher beam energies in general result in an improved spatial resolution, they are not in general preferable, due to the increased noise from straggling, and the increased loss of primaries. Hence, rather than the highest energies, a tradeoff between noise and spatial resolution needs to be defined.

References

1. Agostinelli, S., Allison, J., et al. (2003). GEANT4—a simulation toolkit. Nuclear instruments and methods in physics research section A: Accelerators, Spectrometers, Detectors and Associated Equipment, 506(3), 250-303.

2. Allison, J., Amako, K., et al. (2016). Recent developments in Geant4. Nuclear Instruments and Methods in Physics Research Section A: Accelerators, Spectrometers, Detectors and Associated Equipment, 835, 186-225.

3. Allison, J., Amako, K., et al. (2006). Geant4 developments and applications. IEEE Transactions on nuclear science, 53(1), 270-278.

4. Amaldi, U., Bianchi, A., et al. (2011). Construction, test and operation of a proton range radiography system. Nuclear Instruments and Methods in Physics Research Section A: Accelerators, Spectrometers, Detectors and Associated Equipment, 629(1), 337-344.

5. Amato, C., Martisikova, M., & Gehrke, T. (2020). A technique for spatial resolution improvement in helium-beam radiography. Medical Physics.

6. Barkas, W. H. (1973). Nuclear research emulsions.

7. Bashkirov, V. A., Johnson, R. P., Sadrozinski, H. F. W., & Schulte, R. W. (2016). Development of proton computed tomography detectors for applications in hadron therapy. Nuclear Instruments and Methods in Physics Research Section A: Accelerators, Spectrometers, Detectors and Associated Equipment, 809, 120-129.

8. Bashkirov, V. A., Schulte, R. W., et al. (2016). Novel scintillation detector design and performance for proton radiography and computed tomography. Medical physics, 43(2), 664-674.

9. Beaulieu, L., & Beddar, S. (2016). Review of plastic and liquid scintillation dosimetry for photon, electron, and proton therapy. Physics in Medicine & Biology, 61(20), R305.

10. Bentzen, S. M. (1983). Evaluation of the spatial resolution of a CT scanner by direct analysis of the edge response function. Medical physics, 10(5), 579-581.

11. Berger, M. J., Inokuti, M., et al. (1993). Report 49. Journal of the International Commission on Radiation Units and Measurements, (2), NP-NP.

12. Bregman, L. M. (1965). The method of successive projection for finding a common point of convex sets. Sov. Math. Dok., 162(3), 688-692.

13. Brun, R., & Rademakers, F. (1997). ROOT—an object oriented data analysis framework. Nuclear Instruments and Methods in Physics Research Section A: Accelerators, Spectrometers, Detectors and Associated Equipment, 389(1-2), 81-86.

14. Bucciantonio, M., Amaldi, U., Kieffer, R., Sauli, F., & Watts, D. (2013). Development of a fast proton range radiography system for quality assurance in hadrontherapy. Nuclear Instruments and Methods in Physics Research Section A: Accelerators, Spectrometers, Detectors and Associated Equipment, 732, 564-567.

15. Censor, Y., Elfving, T., Herman, G. T., & Nikazad, T. (2008). On diagonally relaxed orthogonal projection methods. SIAM Journal on Scientific Computing, 30(1), 473-504.

16. Chegg Study, https://www.chegg.com/homework-help/questions-and-answers/using-bethe-bloch-formula-calculate-mass-stopping-power-46-mev-proton-water-estimate-range q18568912. Retrieved 30 May 2020.

17. Choi, T. (2002). IKONOS satellite on orbit modulation transfer function (MTF) measurement using edge and pulse method (Doctoral dissertation, Electrical Engineering Department, South Dakota State University).

18. Collins-Fekete, C. A., Brousmiche, S., Hansen, D. C., Beaulieu, L., & Seco, J. (2017). Pre-treatment patient-specific stopping power by combining list-mode proton radiography and x-ray CT. Physics in Medicine & Biology, 62(17), 6836.

19. Collins-Fekete, C. A., Brousmiche, S., Portillo, S. K., Beaulieu, L., & Seco, J. (2016). A maximum likelihood method for high resolution proton radiography/proton CT. Physics in Medicine & Biology, 61(23), 8232.

20. Collins-Fekete, C. A., Dikaios, N., Royle, G., & Evans, P. M. (2020). Statistical limitations in proton imaging. Physics in Medicine & Biology, 65(8), 085011.

21. Collins-Fekete, C. A., Volz, L., Portillo, S. K., Beaulieu, L., & Seco, J. (2017). A theoretical framework to predict the most likely ion path in particle imaging. Physics in Medicine & Biology, 62(5), 1777.

22. Cunningham, I. A., & Reid, B. K. (1992). Signal and noise in modulation transfer function determinations using the slit, wire, and edge techniques. Medical physics, 19(4), 1037-1044.

23. Depauw, N., & Seco, J. (2011). Sensitivity study of proton radiography and comparison with kV and MV x-ray imaging using GEANT4 Monte Carlo simulations. Physics in Medicine & Biology, 56(8), 2407.

24. DeVries, R. M., & Peng, J. C. (1980). Nucleus-nucleus total reaction cross sections. Physical Review C, 22(3), 1055.

25. Dickmann, J., Wesp, P., et al. (2019). Prediction of image noise contributions in proton computed tomography and comparison to measurements. Physics in Medicine & Biology, 64(14), 145016.

26. Durante, M., & Paganetti, H. (2016). Nuclear physics in particle therapy: a review. Reports on Progress in Physics, 79(9), 096702.

27. Eyges, L. (1948). Multiple scattering with energy loss. Physical Review, 74(10), 1534.

28. Faddegon, B., Ramos-Méndez, J., Schuemann, J., McNamara, A., Shin, J., Perl, J., & Paganetti, H. (2020). The TOPAS tool for particle simulation, a Monte Carlo simulation tool for physics, biology and clinical research. Physica Medica, 72, 114-121.

29. Fekete, C. A. C., Doolan, P., Dias, M. F., Beaulieu, L., & Seco, J. (2015). Developing a phenomenological model of the proton trajectory within a heterogeneous medium required for proton imaging. Physics in Medicine & Biology, 60(13), 5071.

30. Fujita, H., Tsai, D. Y., Itoh, T., Doi, K., Morishita, J., Ueda, K., & Ohtsuka, A. (1992). A simple method for determining the modulation transfer function in digital radiography. IEEE Transactions on medical imaging, 11(1), 34-39.

31. Gallo, G., Presti, D. L., et al. (2016). QBeRT: an innovative instrument for qualification of particle beam in real-time. Journal of Instrumentation, 11(11), C11014.

32. Gehrke, T., Amato, C., Berke, S., & Martišíková, M. (2018). Theoretical and experimental comparison of proton and helium-beam radiography using silicon pixel detectors. Physics in Medicine & Biology, 63(3), 035037.

33. Gehrke, T., Gallas, R., Jäkel, O., & Martišíková, M. (2018). Proof of principle of helium-beam radiography using silicon pixel detectors for energy deposition measurement, identification, and tracking of single ions. Medical physics, 45(2), 817-829.

34. Giacometti, V., Guatelli, S., Bazalova-Carter, M., Rosenfeld, A. B., & Schulte, R. W. (2017). Development of a high resolution voxelised head phantom for medical physics applications. Physica Medica, 33, 182-188.

35. Gordon, R., Bender, R., & Herman, G. T. (1970). Algebraic reconstruction techniques (ART) for three-dimensional electron microscopy and X-ray photography. Journal of theoretical Biology, 29(3), 471-481.

36. Gottschalk, B. (2010). On the scattering power of radiotherapy protons. Medical physics, 37(1), 352-367.

37. Gottschalk, B. (2012). Techniques of proton radiotherapy: transport theory. arXiv preprint arXiv:1204.4470.

38. Gottschalk, B., Cascio, E. W., Daartz, J., & Wagner, M. S. (2015). On the nuclear halo of a proton pencil beam stopping in water. Physics in Medicine & Biology, 60(14), 5627.

39. Groom, D. E., & Klein, S. R. (2000). Passage of particles through matter. The European Physical Journal C-Particles and Fields, 15(1-4), 163-173.

40. Grün, R., Friedrich, T., Krämer, M., Zink, K., Durante, M., Engenhart-Cabillic, R., & Scholz, M. (2015). Assessment of potential advantages of relevant ions for particle therapy: a model based study. Medical physics, 42(2), 1037-1047.

41. Haettner, E., Iwase, H., Krämer, M., Kraft, G., & Schardt, D. (2013). Experimental study of nuclear fragmentation of 200 and 400 MeV/u 12C ions in water for applications in particle therapy. Physics in Medicine & Biology, 58(23), 8265.

42. Hansen, D. C., Bassler, N., Sørensen, T. S., & Seco, J. (2014). The image quality of ion computed tomography at clinical imaging dose levels. Medical physics, 41(11), 111908.

43. Hanson, K. M., Bradbury, J. N., et al. (1981). Computed tomography using proton energy loss. Physics in Medicine & Biology, 26(6), 965.

44. Horst, F., Aricò, G., et al. (2019). Measurement of He 4 charge-and mass-changing cross sections on H, C, O, and Si targets in the energy range 70–220 MeV/u for radiation transport calculations in ion-beam therapy. Physical Review C, 99(1), 014603.

45. Hurley, R. F., Schulte, R. W., et al. (2012). Water-equivalent path length calibration of a prototype proton CT scanner. Medical physics, 39(5), 2438-2446.

46. Hwang, H., Choi, Y. W., Kwak, S., Kim, M., & Park, W. (2008, October). MTF assessment of high resolution satellite images using ISO 12233 slanted-edge method. In Image and Signal Processing for Remote Sensing XIV (Vol. 7109, p. 710905). International Society for Optics and Photonics.

47. Johnson, R. P. (2017). Review of medical radiography and tomography with proton beams. Reports on progress in physics, 81(1), 016701.

48. Judy, P. F. (1976). The line spread function and modulation transfer function of a computed tomographic scanner. Medical physics, 3(4), 233-236.

49. Kanematsu, N., Akagi, T., et al. (1998). A proton dose calculation code for treatment planning based on the pencil beam algorithm. Japanese Journal of Medical Physics, 18(1), 88-103.

50. Kanematsu, N. (2008). Alternative scattering power for Gaussian beam model of heavy charged particles. Nuclear Instruments and Methods in Physics Research Section B: Beam Interactions with Materials and Atoms, 266(23), 5056-5062.

51. Karczmarz, S. (1937). Angenaherte auflosung von systemen linearer glei-chungen. Bull. Int. Acad. Pol. Sic. Let., Cl. Sci. Math. Nat., 355-357.

52. Knopf, A. C., & Lomax, A. (2013). In vivo proton range verification: a review. Physics in Medicine & Biology, 58(15), R131.

53. Kox, S., Gamp, A., et al. (1987). Trends of total reaction cross sections for heavy ion collisions in the intermediate energy range. Physical Review C, 35(5), 1678.

54. Krah, N., Khellaf, F., Létang, J. M., Rit, S., & Rinaldi, I. (2018). A comprehensive theoretical comparison of proton imaging set-ups in terms of spatial resolution. Physics in Medicine & Biology, 63(13), 135013.

55. Lashansky, S. N., Mansbach, S., Berger, M. J., Karasik, T., & Bin-Nun, M. (2008, April). Edge response revisited. In Infrared Imaging Systems: Design, Analysis, Modeling, and Testing XIX (Vol. 6941, p. 69410Z). International Society for Optics and Photonics.

56. Llopart, X., Ballabriga, R., Campbell, M., Tlustos, L., & Wong, W. (2007). Timepix, a 65k programmable pixel readout chip for arrival time, energy and/or photon counting measurements. Nuclear Instruments and Methods in Physics Research Section A: Accelerators, Spectrometers, Detectors and Associated Equipment, 581(1-2), 485-494.

57. Moliere, G. (1947). Theorie der streuung schneller geladener teilchen i. einzelstreuung am abgeschirmten coulomb-feld. Zeitschrift für Naturforschung A, 2(3), 133-145.

58. Moliere, G. (1948). Theorie der streuung schneller geladener teilchen ii mehrfach-und vielfachstreuung. Zeitschrift für Naturforschung A, 3(2), 78-97.

59. Nijhawan, O. P., Gupta, S. K., & Hradaynath, R. (1983). Polychromatic MTF of electrostatic point symmetric electron lenses. Applied optics, 22(16), 2453-2455.

60. Olson, J. T., Espinola, R. L., & Jacobs, E. L. (2007). Comparison of tilted slit and tilted edge superresolution modulation transfer function techniques. Optical Engineering, 46(1), 016403.

61. Paganetti, H. (2009). Dose to water versus dose to medium in proton beam therapy. Physics in Medicine & Biology, 54(14), 4399.

62. Paganetti, H. (2012). Range uncertainties in proton therapy and the role of Monte Carlo simulations. Physics in Medicine & Biology, 57(11), R99.

63. Payne, M. G. (1969). Energy straggling of heavy charged particles in thick absorbers. Physical Review, 185(2), 611.

64. Pemler, P., Besserer, J., et al. (1999). A detector system for proton radiography on the gantry of the Paul-Scherrer-Institute. Nuclear Instruments and Methods in Physics Research Section A: Accelerators, Spectrometers, Detectors and Associated Equipment, 432(2-3), 483-495.

65. Penfold, S. N., Schulte, R. W., Censor, Y., & Rosenfeld, A. B. (2010). Total variation superiorization schemes in proton computed tomography image reconstruction. Medical physics, 37(11), 5887-5895.

66. Perl, J. (2013). TOPAS Tool for Particle Simulation (No. TOPAS; 002932MLTPL00). SLAC National Acceleratory Laboratory.

67. Perl, J., Shin, J., Schümann, J., Faddegon, B., & Paganetti, H. (2012). TOPAS: an innovative proton Monte Carlo platform for research and clinical applications. Medical physics, 39(11), 6818-6837.

68. Piersimoni, P., Ramos-Méndez, J., Geoghegan, T., Bashkirov, V. A., Schulte, R. W., & Faddegon, B. A. (2017). The effect of beam purity and scanner complexity on proton CT accuracy. Medical physics, 44(1), 284-298.

69. Piersimoni, P., Faddegon, B. A., Méndez, J. R., Schulte, R. W., Volz, L., & Seco, J. (2018). Helium CT: Monte Carlo simulation results for an ideal source and detector with comparison to proton CT. Medical physics, 45(7), 3264-3274.

70. Plautz, T., Bashkirov, V., et al. (2014). 200 MeV proton radiography studies with a hand phantom using a prototype proton CT scanner. IEEE transactions on medical imaging, 33(4), 875-881.

71. Poludniowski, G., Allinson, N. M., & Evans, P. M. (2015). Proton radiography and tomography with application to proton therapy. The British journal of radiology, 88(1053), 20150134.

72. Presti, D. L., Bonanno, D. L., et al. (2016). Design and characterisation of a real time proton and carbon ion radiography system based on scintillating optical fibres. Physica Medica, 32(9), 1124-1134.

73. Rit, S., Freud, N., Sarrut, D., & Létang, J. M. (2012, May). Distance-driven binning for proton CT filtered backprojection along most likely paths. In Second International Conference on Image Formation in X-Ray Computed Tomography, Conference Paper.

74. Rossi, B., & Greisen, K. (1941). Cosmic-ray theory. Reviews of Modern Physics, 13(4), 240.

75. Rovituso, M., Schuy, C., et al. (2017). Fragmentation of 120 and 200 MeV u− 1 4He ions in water and PMMA targets. Physics in Medicine & Biology, 62(4), 1310.

76. Sadrozinski, H. W., Geoghegan, T., et al. (2016). Operation of the preclinical head scanner for proton CT. Nuclear Instruments and Methods in Physics Research Section A: Accelerators, Spectrometers, Detectors and Associated Equipment, 831, 394-399.

77. Sauli, F. (1997). GEM: A new concept for electron amplification in gas detectors. Nuclear Instruments and Methods in Physics Research Section A: Accelerators, Spectrometers, Detectors and Associated Equipment, 386(2-3), 531-534.

78. Schardt, D., Elsässer, T., & Schulz-Ertner, D. (2010). Heavy-ion tumor therapy: Physical and radiobiological benefits. Reviews of modern physics, 82(1), 383.

79. Schneider, U., & Pedroni, E. (1994). Multiple Coulomb scattering and spatial resolution in proton radiography. Medical physics, 21(11), 1657-1663.

80. Schulte, R. W., Bashkirov, V., et al. (2005). Density resolution of proton computed tomography. Medical physics, 32(4), 1035-1046.

81. Schulte, R. W., Penfold, S. N., Tafas, J. T., & Schubert, K. E. (2008). A maximum likelihood proton path formalism for application in proton computed tomography. Medical physics, 35(11), 4849-4856.

82. Smith, S. W. (1997). The scientist and engineer's guide to digital signal processing.

83. Talamonti, C., Reggioli, V., et al. (2010). Proton radiography for clinical applications. Nuclear Instruments and Methods in Physics Research Section A: Accelerators, Spectrometers, Detectors and Associated Equipment, 612(3), 571-575.

84. The International System of Units (SI) (PDF). Bureau International des Poids et Mesures (BIPM). Retrieved 2010-01-31.

85. Trikalinos, T. A., Terasawa, T., Ip, S., Raman, G., & Lau, J. (2009). Particle beam radiation therapies for cancer.

86. Tzannes, A. P., & Mooney, J. M. (1995). Measurement of the modulation transfer function of infrared cameras. Optical Engineering, 34(6), 1808-1818.

87. Ulmer, W., & Matsinos, E. (2010). Theoretical methods for the calculation of Bragg curves and 3D distributions of proton beams. The European Physical Journal Special Topics, 190(1), 1-81.

88. Volz, L., Collins-Fekete, C. A., Piersimoni, P., Johnson, R. P., Bashkirov, V., Schulte, R., & Seco, J. (2017). Stopping power accuracy and achievable spatial resolution of helium ion imaging using a prototype particle CT detector system. Current Directions in Biomedical Engineering, 3(2), 401-404.

89. Volz, L., Collins-Fekete, C. A., Solie, J. R., & Seco, J. (2020). Theoretical considerations on the spatial resolution limit of single-event proton radiography. Biomedical Physics & Engineering Express.

90. Volz, L. (2020). Particle imaging for daily in-room image guidance in particle therapy. PhD Thesis, Heidelberg University.

91. Volz, L. (2017). Theoretical and Experimental Investigation of Charged Particle Imaging. (Master Thesis). University of Heidelberg. Heidelberg, Germany.

92. Volz, L., Piersimoni, P., et al. (2018). The impact of secondary fragments on the image quality of helium ion imaging. Physics in Medicine & Biology, 63(19), 195016.

93. Volz, L., Piersimoni, P., Johnson, R. P., Bashkirov, V. A., Schulte, R. W., & Seco, J. (2019). Improving single-event proton CT by removing nuclear interaction events within the energy/range detector. Physics in Medicine & Biology, 64(15), 15NT01.

94. a

95. Weber, U., & Kraft, G. (2009). Comparison of carbon ions versus protons. The Cancer Journal, 15(4), 325-332.

96. What Is Radiotherapy, What is Radiotherapy? Benefits and Side Effects- TROG Cancer Research, https://www.trog.com.au/What-is-radiotherapy; 2013, [accessed 9 May 2020].

97. Williams, D. C. (2004). The most likely path of an energetic charged particle through a uniform medium. Physics in Medicine & Biology, 49(13), 2899.

98. World Health Organization Cancer, World Health Organization, https://www.who.int/news-room/fact-sheets/detail/cancer; 2018, [accessed 2 January 2020].

99. Worstell, W. A., Adams, B. W., et al. (2019, March). First results developing time-of-flight proton radiography for proton therapy applications. In Medical Imaging 2019: Physics of Medical Imaging (Vol. 10948, p. 109480G). International Society for Optics and Photonics.

100. Yin, F. F., Giger, M. L., & Doi, K. (1990). Measurement of the presampling modulation transfer function of film digitizers using a curve fitting technique. Medical physics, 17(6), 962-966.

101. Ziegler, J. F., Ziegler, M. D., & Biersack, J. P. (2010). SRIM–The stopping and range of ions in matter (2010). Nuclear Instruments and Methods in Physics Research Section B: Beam Interactions with Materials and Atoms, 268(11-12), 1818-1823.